ISSN: 2175 9146

# JOURNAL OF AEROSPACE TECHNOLOGY AND MANAGEMENT

VOLUME NO. 15
ISSUE NO. 1
JANUARY - APRIL 2023


**ENRICHED PUBLICATIONS PVT. LTD**

**S-9, IInd FLOOR, MLU POCKET,
MANISH ABHINAV PLAZA-II, ABOVE FEDERAL BANK,
PLOT NO-5, SECTOR-5, DWARKA, NEW DELHI, INDIA-110075,
PHONE: - + (91)-(11)-47026006**

ISSN: 2175 9146

# Journal of Aerospace Technology and Management

**Aims and Scope**

The Journal of Aerospace Technology and Management (JATM) is an open-access journal devoted to research and management on different aspects of aerospace technologies.

For all accepted manuscripts, the correspondence author will be asked to contribute with the Article Processing Charge, which will be applied to editorial services that support the publishing process, like editing, proofreading, indexing and dissemination.

The value is fixed per article, independent of its length and is R$ 800,00 (in Brazilian reais) or U$300,00 (in American dollars). In exceptional cases, the editorial board may waive a contribution upon reasonable request.

JATM accepts manuscripts already published in preprint, considered reliable by the editorial committee, and must be informed in the Open Science Compliance Form that must be submitted as a supplementary file to the Manuscript.

ISSN: 2175 9146

# Journal of Aerospace Technology and Management

## EDITORS IN CHIEF

ISSN: 2175 9146

# Journal of Aerospace Technology and Management

(Volume No. 15, Issue No. 1, January - April 2023)

## Contents

# Performance Enhancement of a Solar Air Collector Using a V-Corrugated Absorber

**Angham Fadil Abed1 , Ruaa Braz Dahham2 , Noora Abdul Wahid Hashim1,* , Raisan Faris Hamad1**

1.University of Kufa – Engineering Faculty – Mechanical Engineering Department – Najaf – Iraq.
2.Directorate General of Education – Kufa/Najaf – Iraq.

## ABSTRACT

*Solar energy is one of the most efficient forms of renewable energy. Solar air collectors are promising utilization of solar energy. The present study used unsteady three-dimensional Computational Fluid Dynamic (CFD) analysis to investigate the heat transfer and fluid friction in solar air collectors with smooth and v-corrugation absorber plates. The studied parameters are Reynolds number, v-corrugation height, and pitch. Three Reynolds number (500, 1000, 1500) values were used with three arrangements configuration of the v-corrugation of relative heights of 0.10, 0.16, and 0.23. Roughness pitches varied between 1.33, 1.66, and 2. By comparing the simulated thermal efficiency with the currently known experimental values, great agreement can be approved. Results show the superiority of the performance of v-corrugated collector against the traditional or smooth type. The outlet temperature obtained in case of relative roughness height = 0.23 and relative roughness pitch = 2 is 61 °C, while it is 53 °C for a smooth type. Also, a higher thermal efficiency of 46.7 % can be obtained compared to 33.01% for smooth type.*

***Keywords: Nusselt number; Solar air collector; CFD; Friction factor; Thermal efficiency***

## I. INTRODUCTION

Every day, energy demand grows. There are many distinct types of energy resources, including major and minor, renewable and non-renewable, commercial and non-commercial energies. Solar energy is one of the most practical forms of renewable energy. It has been regarded as a large and cost-effective energy source due to its abundance. Also it can be harnessed after years of research. Solar air collector systems were created with the primary goal of gathering as much heat energy as possible while reducing pumping costs. In order to decrease the consumption of oil, gas, electricity, and other equivalent sources of heat, several different forms of solar heating systems have been devised (Kumar et al. 2017).

One of the most promising uses for air solar collectors is providing hot air for drying agricultural and marine products, or air conditioning processes especially in winter. In these devices, solar energy is converted to heat which is transferred to air. The most prevalent solar collectors used for domestic water heating are the flat-plate collectors. Compared to solar water collectors, air collectors are less expensive and require less maintenance. A traditional flat-plate collector is a metal box insulated with a plastic or glass lid (termed as the glazing) with an absorber of dark color. Lower than 80 °C temperatures can be

used to heat liquids or air. Traditional collectors have a lower thermal efficiency because of low heat transfer convective coefficient through the absorber and the moving air stream (Amraoui and Aliane 2018; Yadav and Bhagoria 2013). By adding baffles or other impediments to the absorber surface of the collectors, altering number of covers and passes of flow, dual glassing, or making corrugation in the absorber, the system's thermal performance can be enhanced. As a result, the absorber and the coefficients of air heat transfer will be higher (Hakam et al. 2016; Hedayatizadeh et al. 2016). Numerous researches have focused into the impact of various roughness geometries of absorber on heat transfer. Numerical research of solar sloped collectors was carried out by Varol and Oztop (2007). The results showed that transfer of heat increased with increasing aspect ratio and Rayleigh number but decreased when length of wave increased. Chaube et al. (2006) employed CFD to predict the improvement of heat transfer and characteristics of flow based on the rib-roughed absorber surface of a 2D air solar heater. Karmare and Tikekar (2010) used Ansys Fluent to optimize numerically the geometric design of various metal rib shapes for heat transmission of an absorber in air solar heater. The rib height and width of 2 mm, relative width gap of 1, relative pitch gap of 0.25, and Re ranging from (3000 to 18, 000 ) in rectangular air solar heater. Heat transfer improvement carried on by inclined gap with continuous rib arrangement was investigated by Aharwal et al. (2008). They found that the friction factor and Nusselt number increased by 2.2-2.87 and 1.48-2.59 times, respectively, compared with smooth collectors. Karmare and Tikekar (2010) utilized CFD to quickly and economically assess flow of fluid and transmission of heat in air solar heaters. A collection plate with 600 ribs in the forms of circles, squares, and triangles was used in their experiment. The direction of the airflow was inclined. On the surface, the ribs were staggered out in a specified grid. The ribs maximized heat transfer due to their square cross-section and 580 angle of attack. When a square plate was utilized instead of one with a smooth surface, heat transmission is improved by 30%. Chaichan et al. (2016) raised the temperature of the surrounding air by nearly 101 percent using an aluminum flat plate installed in a 1 m2 opaque heater Solar Air Collector (SAC). The stream of air entered from top and exited from bottom of the collector. The researchers showed that by absorbing heat from solar radiation, an aluminum absorber may be used as a heating source which was essential to augment the thermal performance of the solar heater. Darici and Kilic (2020) combined two SAC, an absorber corrugate in the form of trapezoidal and another flat absorber. They examined how SAC thermal efficiency was impacted by the absorber form and air mass flow rate. There were used three rate values of mass flow for air: 0.022, 0.033, and 0.044 kg/s. Results indicated that when the rate of mass flow was reduced, SAC output temperature increased. The highest difference of temperature in the SAC with a trapezoidal absorber was about 9 °C greater than in flat absorber at a mass rate of 0.022 kg/s. SAC thermal performance increased as the rate of mass flow increased when employing the trapezoidal absorber plate at 0.044 kg/s, with a daily average thermal efficiency about 63%. Zheng et al. (2017) created mathematical models to evaluate the thermal

l performance of corrugated model SAC in cold-climate environments. In contrast to the temperature of the input air and the width of the corrugated plate, the collector thermal efficiency decreased as the corrugation height, surface area, intensity of radiation, velocity of air, and temperature of ambient were increased. Both exegetical and thermal efficiency attained 73 percent. Manjunath et al. (2018) used a CFD analysis for a SAC with sinusoidal shape absorber. The values of Re used were 4,000 to 24,000. In comparison to a typical air solar collector with a smooth plate, their studies showed that sinusoidal waves greatly increased heat transmission and improved flow disturbances, leading to an increase in average thermal efficiency by 12.5%. To enhance thermal performance in a solar heat exchanger duct, Promvonge et al. (2022) tested a newly developed louver punched V-baffle (LPVB) vortex generator analytically and experimentally. Air was employed in the test fluid, flowing through the continuously heated duct at Reynolds numbers (Re) ranging from 5,300 to 23,000. According to their research, the LPVB with PR (relative baffle pitches) = 1.5, (louver angle) = 45°, and LR (relative louver size) = 0.9 performs at its best. Two semi cylinders, two flexible baffles, and alternately attached lower and upper channel walls were used in Salih et al. (2023) study of a forced fluid flowing inside a horizontal channel. The semi-cylinders, which are heated by constant temperature, are filled with a phase-change substance. While the pressure drop throughout the channel significantly diminishes, the Nusselt number is only marginally (0.9%) increased by the flexible baffles with a lower modulus of elasticity.

Based on the previous survey of the literature, it appears that relatively little researches employed a 3D transient numerical studies analysis with variable climatic conditions of artificially roughened SAC having an absorber in the form of v-corrugated plate, which makes the present work novel. Using a unique CFD analysis, the current work intends to fill a knowledge gap by systematically analyzing the unsteady, 3D flow and influence of v-corrugated absorber on heat transmission and fluid friction in SAC. Additionally, this work examines the change of meteorological factors, including solar radiation, temperature of environment, wind velocity, and temperature of inlet air, and how these parameters affected the effectiveness of various solar air collectors' arrangement (smooth absorber plate SAC and v-corrugated absorber plate SAC). This study's main objective is to find out how air solar collectors' average Nusselt number, average friction factor, and thermal performance are influenced by factors like Re, relative roughness height (e/H), and relative roughness pitch (p/H) of absorber plates. In order to establish a parametric investigation, a v-corrugated absorber plate SAC was compared to a smooth flat plate SAC using COMSOL SOFTWARE V5.5.

## MODEL DESCRIPTION

A schematic of the three-dimensional SACs are displayed in Fig. 1, which has a conventional flat plate SAC (smooth absorber plate SAC). A collection of equal-sided triangles makes up the v-corrugated plate geometry. The SAC is a box of metal with a bottom made of dark-colored aluminum absorber

r plates, a top made of extremely transparent, anti-reflective glass called glazing, and a space between them. The bottom surface of the absorber is insulated by using a glass wool layer to prevent losses of heat. Air temperature rises as a result of heat transfer of the absorber caused by solar radiation that penetrates the glassing layer, falls on the absorber, and causes increase in temperature. The collector length and width are 1.2 m, 0.3 m, respectively. The other geometric specifications for the present SAC are shown in Table 1. CFD simulations are conducted using various collections of height (e), pitch (p), and Re. Each configuration of collectors is examined at three distinct values of Re ranging (500, 1000, 1500) corresponding to rates of mass flow

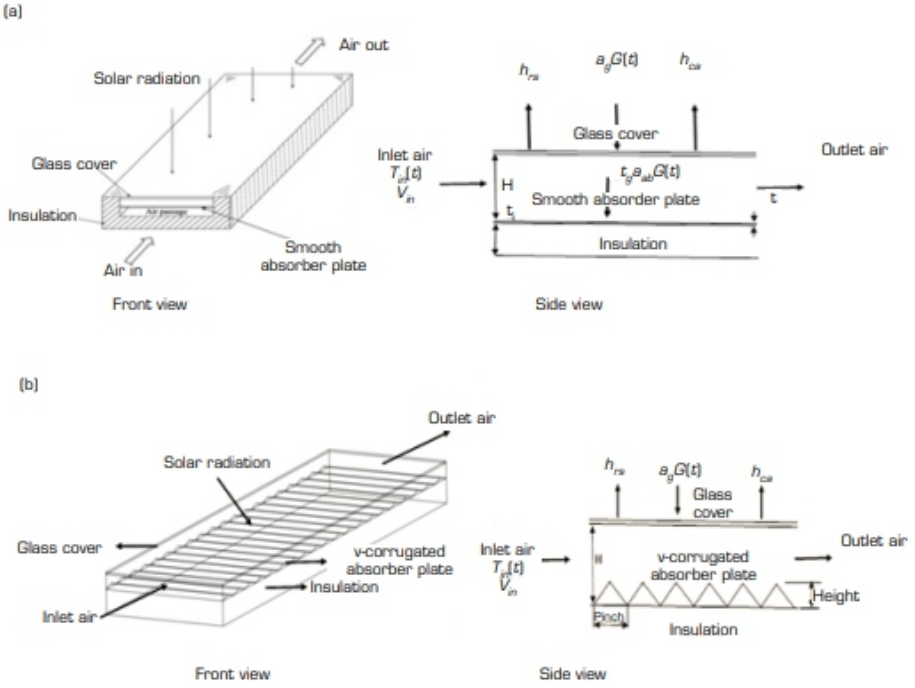


Source: Elaborated by the authors.

**Figure 1.** Thermal schematics of the solar air collectors. (a) Smooth absorber SAC; (b) V-corrugated absorber SAC.

**Table 1.** Criteria for solar air collectors' geometry.

| Parameter | Value | Parameter | Value |
|---|---|---|---|
| Absorber plate thickness, $t$ (m) | 0.001 | $e$(m) | 0.003, 0.005, 0.007 |
| Duct height $H$ (m) | 0.03 | $p$(mm) | 0.04, 0.05, 0.06 |
| Insulation thickness, $t_i$ (m) | 0.01 | $e/H$ | 0.10, 0.16, 0.23 |
| Glass layer thickness (m) | 0.004 | $p/H$ | 1.33, 1.66, 2 |
| Hydraulic diameter, $D_h$ (m) | 0.05454 | | |

Source: Elaborated by the authors.

## NUMERICALANALYSIS

### CFD Setup and Boundary Conditions

The present study used a model by COMSOL SOFTWARE V.5.5. This software is a robust interactive environment that is used to model and solve science and engineering problems of all kinds. With this

s program, a conventional model for one form of physics can be extended easily to Multiphysics models that simultaneously solve combined physics phenomena. Incompressible three-dimensional transient laminar flow model is considered. The flow is taken as laminar because of low values of inlet air velocity, which depend on ambient speed that ranges from 0.1-0.4 m/s. In contrast to air, whose thermal characteristics vary with temperature, the absorber plate, insulation, and transparent cover all have fixed thermal properties. The convergence limit of relative deviations of continuity, velocity components, and energy are assumed to be, 10-3, 10-3, and 10-6 respectively. The creation of the studied geometry is the initial stage in CFD analysis. A further step is to create a mesh. The input variables are solar radiation G ambient temperature Ta, inlet temperature Tin and wind velocity Vw. The various boundary conditions can be written as follows for both configurations (Fig. 1a and b): At inlet: variable inlet air temperature Tin (t) is taken. Velocity of air is considered uniform at inlet. Re is used to determine the average inlet velocity. At the top clear glass cover, solar radiation flux is applied and will changes during the simulated day, and the outer exchanges from the transparent cover to outside air are convective equal to (hca(Tg – Ta)) and equal to (hrs(Tg – Ts)). The glass cover's transmittance value is 0.9. Heat flux equals to (τg aab G(t)) be applied in upper absorber surface. Aluminum plate heat absorption coefficient is 95 percent, at the lateral and bottom plates, which are designated as a "adiabatic wall" because they are thought to be a good insulation. No-slip condition is applied on all walls. At the channel's outlet, pressure is assumed equal to 101325 Pa. Sky temperature, TS is calculated by the formula used by Winbank (1963) (Eq. 1):

$$T_s = 0.0552 T_a^{1.5} \quad (1)$$

**Governing Equations**

The unsteady incompressible laminar flow in a smooth and v-corrugated plate SAC is governed by the continuity, momentum, and energy equations. The following is a description of the governing equations for three-dimensional transient CFD simulations (Hassan 2022).

Continuity equation (Eq. 2):

$$\frac{\partial \rho}{\partial t} + \frac{\partial u}{\partial x} + \frac{\partial v}{\partial y} + \frac{\partial w}{\partial z} = 0 \quad (2)$$

Momentum equations (Eqs. 3–5) (Hassan 2022):

$$\rho\left(\frac{\partial u}{\partial t}+u\frac{\partial u}{\partial x}+v\frac{\partial u}{\partial y}+w\frac{\partial u}{\partial z}\right)=\rho g_x-\frac{\partial P}{\partial x}+\mu\left(\frac{\partial^2 u}{\partial x^2}+\frac{\partial^2 u}{\partial y^2}+\frac{\partial^2 u}{\partial z^2}\right) \quad (3)$$

$$\rho\left(\frac{\partial v}{\partial t}+u\frac{\partial v}{\partial x}+v\frac{\partial v}{\partial y}+w\frac{\partial v}{\partial z}\right)=\rho g_y-\frac{\partial P}{\partial y}+\mu\left(\frac{\partial^2 v}{\partial x^2}+\frac{\partial^2 v}{\partial y^2}+\frac{\partial^2 v}{\partial z^2}\right) \quad (4)$$

$$\rho\left(\frac{\partial w}{\partial t}+u\frac{\partial w}{\partial x}+v\frac{\partial w}{\partial y}+w\frac{\partial w}{\partial z}\right)=\rho g_z-\frac{\partial P}{\partial z}+\mu\left(\frac{\partial^2 w}{\partial x^2}+\frac{\partial^2 w}{\partial y^2}+\frac{\partial^2 w}{\partial z^2}\right) \quad (5)$$

Energy equation (Eq. 6) (Hassan 2022):

$$\rho C_p\left(\frac{\partial T}{\partial t}+\frac{\partial T}{\partial t}+u\frac{\partial T}{\partial x}+v\frac{\partial T}{\partial y}+w\frac{\partial T}{\partial z}\right)=K\left(\frac{\partial^2 T}{\partial x^2}+\frac{\partial^2 T}{\partial y^2}+\frac{\partial^2 T}{\partial z^2}\right) \quad (6)$$

**Data Reduction and Grid Independence**

In the current CFD model, the average Nusselt number (Nu) , average friction factor (Cf) and average thermal efficiency (ηth) in a smooth and v-corrugation absorber SAC are the primary research interests. For solar air collectors, the average Nu is calculated by Eq. 7 (Choi H and Choi K 2020; Rouissi et al. 2021; Yadav and Bhagoria 2013):

$$Nu=\frac{hD_h}{K} \quad (7)$$

Cf for a SACs (smooth and v-corrugation absorber) is computed by Eq. 8 (Choi H and Choi K 2020; Hassan 2022; Yadav and Bhagoria 2013):

$$Cf=\frac{(\Delta P/l)D_h}{2\rho v^2} \quad (8)$$

The percentage between the thermal power that is actually transferred to air and the maximum theoretical power is referred to as the thermal efficiency of SAC and can be written by Eq. 9 (Rouissi et al. 2021)

$$\eta_{th}=\frac{Q_u}{Q_{max}} \quad (9)$$

where (Eq. 10 and 11)

$$Q_u=\dot{m}C_p\Delta T \quad (10)$$

$$Q_{max}=G(t)S \quad (11)$$

The numerical domain has been discretized using elements in three dimensions. A finer meshing at v-roughened has been done to be able to carefully investigate the flow characteristic and heat transmission in corrugated zones. Table 2 shows the characteristics of the tested meshes. As seen in Fig. 2, coarser mesh has been employed in various places. Near the heating wall, the boundary layers are fastened together. A test of grid independence has been performed in order to reduce computation time while maintaining the precision of the meshes, which is important for the quality of the findings. This test for the average output air temperature of v-corrugated SAC and smooth SAC is shown in Fig. 2b. As a result, the mesh refinement findings show a difference between two sets of data that is less than 2%. Further refining has an impact on the output, but

does not alter it by more than 1.25 percent, therefore this mesh quality is considered suitable for calculation.

**Table 2.** Characteristics of the tested meshes.

| | Mesh size | Domain elements | | Boundary elements | | Edge elements | |
|---|---|---|---|---|---|---|---|
| | | Smooth SAC | v-corrugated SAC | Smooth SAC | v-corrugated SAC | Smooth SAC | v-corrugated SAC |
| 1 | Grid 1 | 50895 | 56502 | 12118 | 14044 | 770 | 1653 |
| 2 | Grid 2 | 104001 | 104541 | 18548 | 20796 | 952 | 2001 |
| 3 | Grid 3 | 234064 | 256391 | 35453 | 40006 | 1289 | 2804 |
| 4 | Grid 4 | 1410114 | 1438827 | 141538 | 150400 | 2505 | 5603 |
| 5 | Grid 5 | 3649021 | 10220004 | 267562 | 629000 | 3423 | 11783 |

**Source:** Elaborated by the authors.

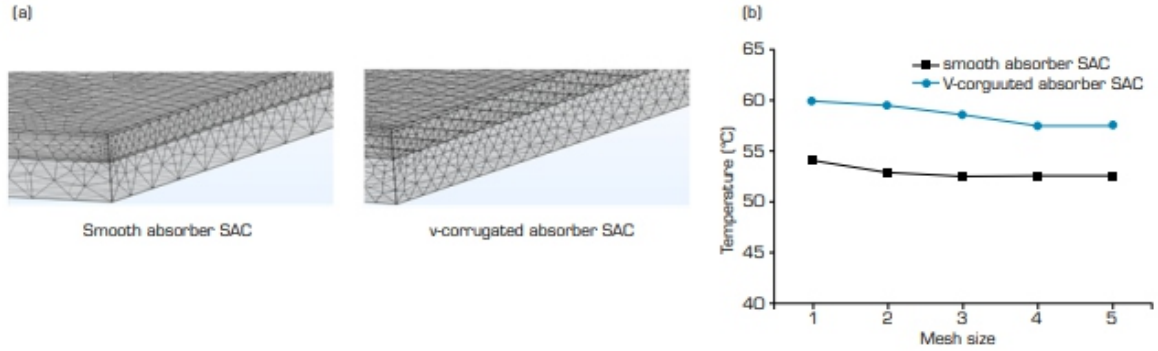


Source: Elaborated by the authors.

**Figure 2.** (a) Mesh of the solar collectors; (b) Grid independency test for outlet air temperature.

### Properties of Air

Air's thermophysical parameters are influenced by pressure, temperature, and humidity. The following thermophysical properties, which hold true for temperature ranges between 280 and 470 K, will be incorporated into the present model for the accuracy of the simulation results

$$\rho = 3.9147 - 0.016082T + 2.9013 \times 10^{-5}T^2 - 1.9407 \times 10^{-5}T^3 \quad (12)$$

$$\mu = (1.6157 + 0.06523T - 3.0297 \times 10^{-5}T^2) \times 10^{-6} \quad (13)$$

$$K = (0.0015215 + 0.097459T - 3.3322 \times 10^{-5}T^2) \times 10^{-3} \quad (14)$$

$$C_p = 1009.26 - 0.0040403T + 0.00061759T^2 - 0.0000004097T^3 \quad (15)$$

## RESULTS AND DISCUSSIONS

### Numerical Results Validation

Thermal efficiency of the smooth absorber SAC is compared with experimental findings provided by Hameed et al. (2021) in order to confirm the CFD outcomes obtained in this work at various air flow rates, as seen in Fig. 3. In the present model, the used climatic variables such as solar radiation, ambient

temperature and wind velocity, are the as in experimental investigation of Hameed et al. (2021) for this validation setup in order to assess and contrast the system's energy performance. The average absolute difference between the experimental and estimated values of thermal efficiency is 6.44 percent.

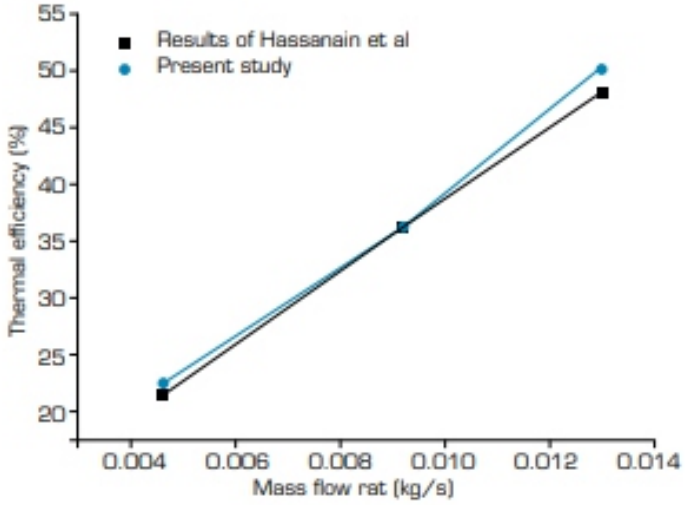


Source: Elaborated by the authors.

**Figure 3.** Average thermal efficiency variation with mass flow rate: a comparison of the experimental research of Hameed *et al.* (2021) and present work.

**Weather Conditions**

The numerical simulation was run on a sunny September day (2/9/2019) at Kufa, Iraq, using experimental climatic data. On a sunny day, the solar radiation intensity peaks between 12:00 and 13:00 and exceeds 1000 W/m2. The outside temperature and wind speed were 40 to 49.7 0C and 0.1 to 0.4 m/s, respectively.

**Velocity and Temperature Distribution**

Figure 4 displays the plots of the temperature distribution contour for the two SAC types (smooth and v-corrugated) at various periods at (Re 1500). As air moves over the hot absorber surface, heat is transmitted to air, and the temperature of moving fluid slowly rises with distance along the duct. As can be seen at 15 p.m. the corrugation in the absorber causes the highest temperature (102oC) in the corrugated collector, but it is 95oC in the smooth, indicating an improvement in the recommended collector. Due to modeling, when using thermal storage of an absorbing plate, the temperature in two collectors is low in the morning (9 a.m.) and starts to rise to high values at around 3 p.m. (the same trend is shown in Naraghi and Blanchard (2015)).

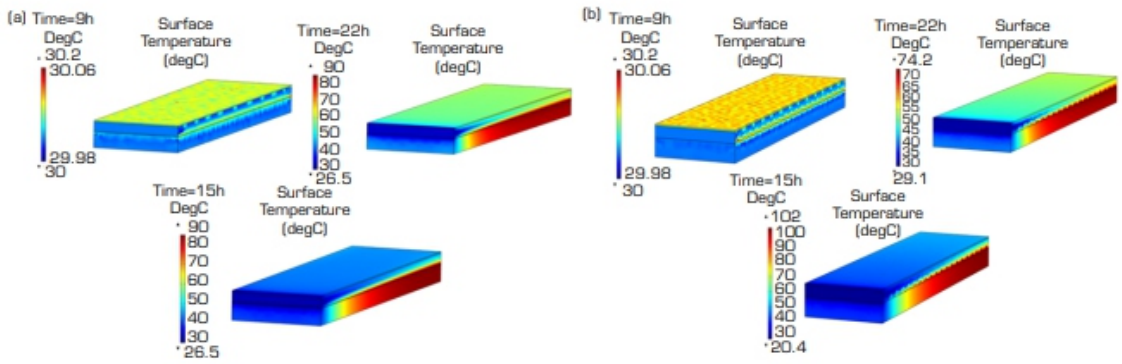


Source: Elaborated by the authors.

**Figure 4.** Temperature distribution for the two collectors. (a) *Re* = 1500 Smooth absorber solar air collector; (b) *Re* = 1500, *e/H* = 0.23 V-corrugated absorber solar air collector.

Figure 5 shows the streamlines and velocity distribution for the smooth and corrugated absorber solar air collectors at values of (e/H = 0.23) and various values of periods for (Re = 1500). Because the flow is expected to be laminar and the velocity increases at the corrugated collector rather than the smooth collector, the airflow is nearly uniform inside the two collectors. The velocity profiles are not comparable, and a corrugated absorber is found to have a higher velocity at a rate of around 1.5 times the inlet velocity. As the sun radiation increased, the magnitude of the velocity increased.

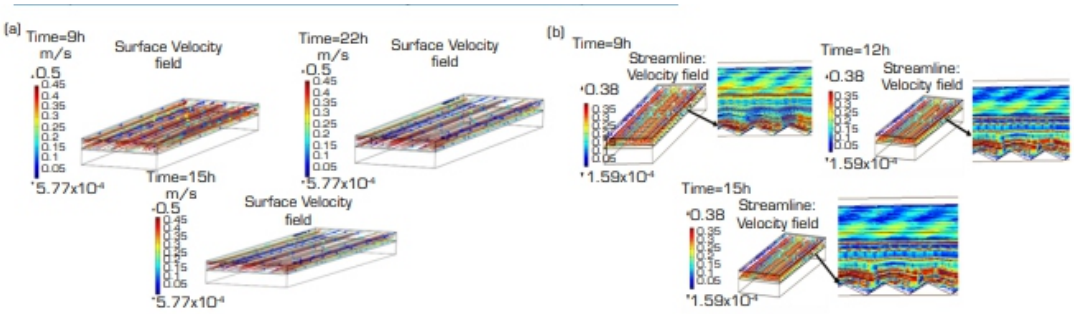


Source: Elaborated by the authors.

**Figure 5.** Streamlines and velocity distribution for the two collectors. (a) *Re* = 1500 smooth absorber solar air collector; (b) *Re* = 1500, *e/H* = 0.23 v- corrugated absorber solar air collector.

## Heat transfer

Figure 6 pares a smooth absorber SAC with a v-corrugated absorber SAC using average Nusselt number and average output air temperature values for various (e/H) and (p/H) as function of Reynolds number. Because the v-corrugation local velocity, the corrugation in the absorber can produce better heat transfer performance than a smooth plate. The results show as Re rises, the average Nu also rises, which improves the transfer rate of heat. For constant values of (p/H) and Re, the average Nugrows when (e/H) increases. This is because, at a given amount of Reynolds number, the local air velocity increases more rapidly as the height (e/H) increases, leading to improved heat transfer performance. It is also evident from the data given, at a fixed value of (e/H) and Re, the average Nu rises as the (p/H) drops. The number

The number of corrugations rises when pitch (p/H) decreases. The flow acceleration area expands as the number of corrugations rises, as a result the average Nu increases. The inclusion of in the absorber enhances the collector area as compared to a smooth duct and a rise in temperature of the outlet air occurs.

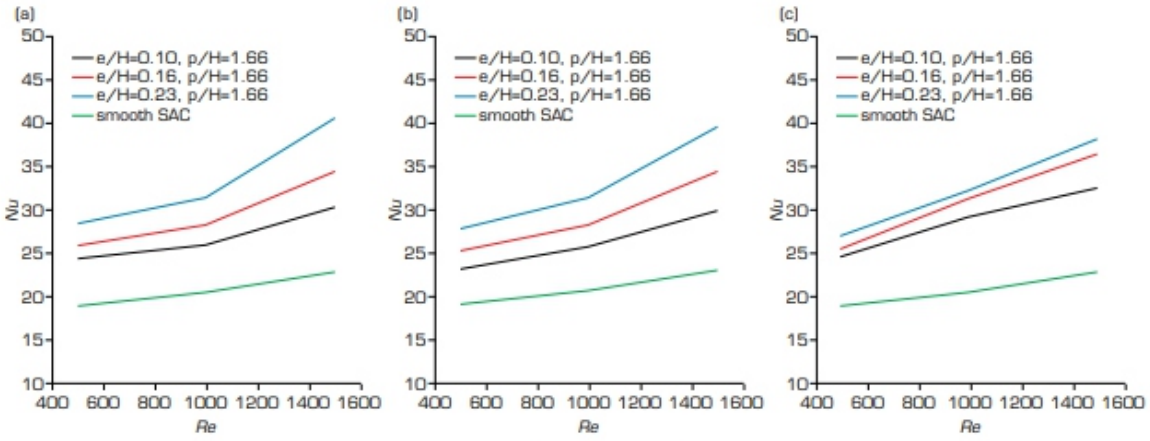


Source: Elaborated by the authors.

**Figure 6.** Average Nusselt number variation for smooth and v-corrugated SACs. (a) (p/H) = with different values of (e/H); (b) (p/H) = with different values of (e/H); (c) (p/H) = with different values of (e/H).

The average outlet air temperature is shown in Fig. 7 as a function of the Re for the chosen values of (e/H) and (p/H). The results demonstrate that, regardless of the shape of the absorber, the outlet temperature will decrease as the Reynold number rises. In addition, it is evident the average temperature of outlet air rises with height (e/H) for a given pitch (p/H) and Reynolds number as discussed above, and is generally higher than smooth because corrugated plates have the significant advantage of better solar radiation absorption than smooth ones, which improve the coefficients of heat transfer between the absorber and the flow of air. As compared to a smooth absorber plate SAC, which has an average temperature of 53 °C, a SAC of (e/H = 0.23 and p/H = 2) achieves a maximum average outlet temperature of roughly 61 °C.

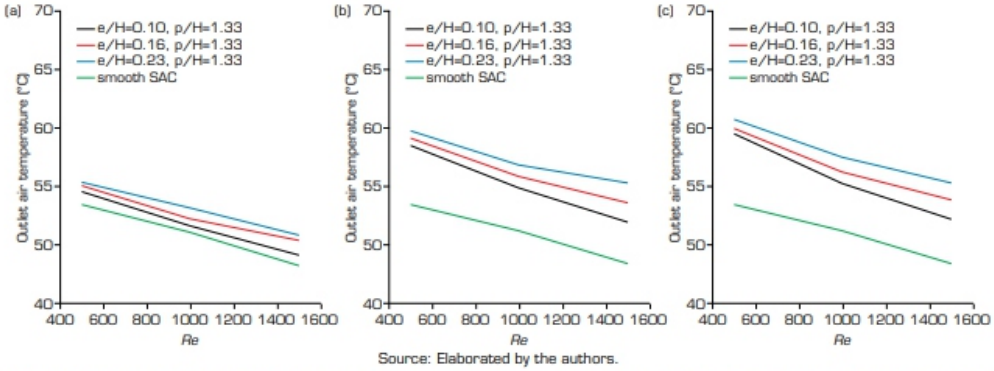


Source: Elaborated by the authors.

**Figure 7.** Variation of average temperature of outlet air for smooth and v-corrugated SACs at different values of height and pitch with Reynolds number. (a) (p/H) = 1.33 with different values of (e/H); (b) (p/H) = with different values of (e/H); (c) (p/H) = with different values of (e/H).

## Friction Loss

One of the great challenges in designing a solar air collector is selecting the suitable parameters like average Nusselt number, average friction factor, and thermal performance of the collector components to achieve the best performance while keeping the lowest cost possible. Figure 8 displays the change of the average friction factor with Re at various heights (e/H) and pitches (p/H) for corrugated and smooth collectors. In every situation, installing v-corrugation causes the average friction factor to be higher than in a smooth collector. The flow is obstructed by the corrugation. The results show that when the Re rises, the average Cf falls. Additionally, it is observed for a given value of the Re and (p/H), the average Cf increases dramatically as the (e/H) increases. It is brought on by the rise in flow route disruptions brought on by the rising value of (e/H). Additionally, it is observed that for fixed values of Re and height (e/H), the average Cf rises as (p/H) decreases. This is due to the fact that as pitch (p/H) drops, the number of corrugation zones grows and more flow blockage results.

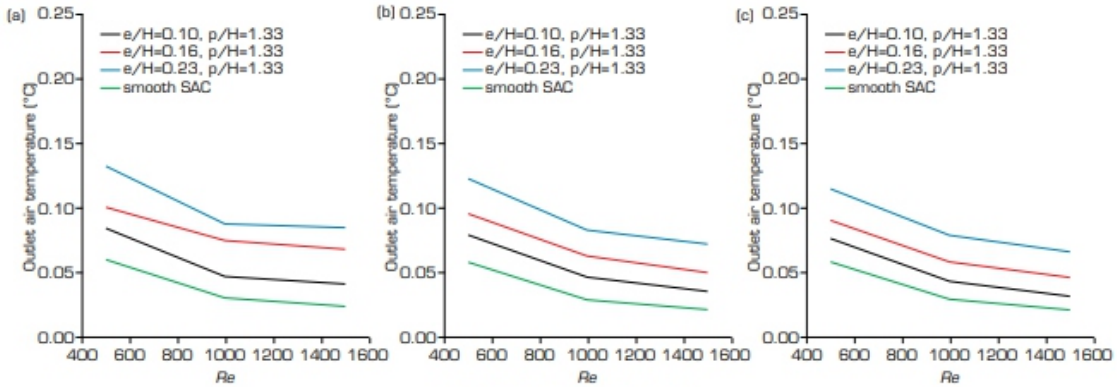


Source: Elaborated by the authors.

**Figure 8.** Variation of average friction factor for smooth SAC and v-corrugation SAC at distinct values of height and pitch with Reynolds number. (a) p/H) = 1.33 with different values of (e/H); (b) p/H) = with different values of (e/H); (c) p/H) = with different values of (e/H).

## Thermal Efficiency

Figure 9 shows the influence of Reynolds number on the average thermal efficiency of the corrugated and smooth SAC during the simulated day. It is demonstrated that the thermal efficiency of the two SAC rises as Reynolds number increases, and that corrugated absorber plates have greater thermal efficiencies than smooth ones. It is discovered that, at a given value of the Re and (p/H), the average thermal efficiency increases dramatically as (e/H) increases. The highest thermal efficiency is seen for (e/H = 0.23), (p/H = 2), and is around 46.7%, as opposed to 33.1% for a smooth collector.

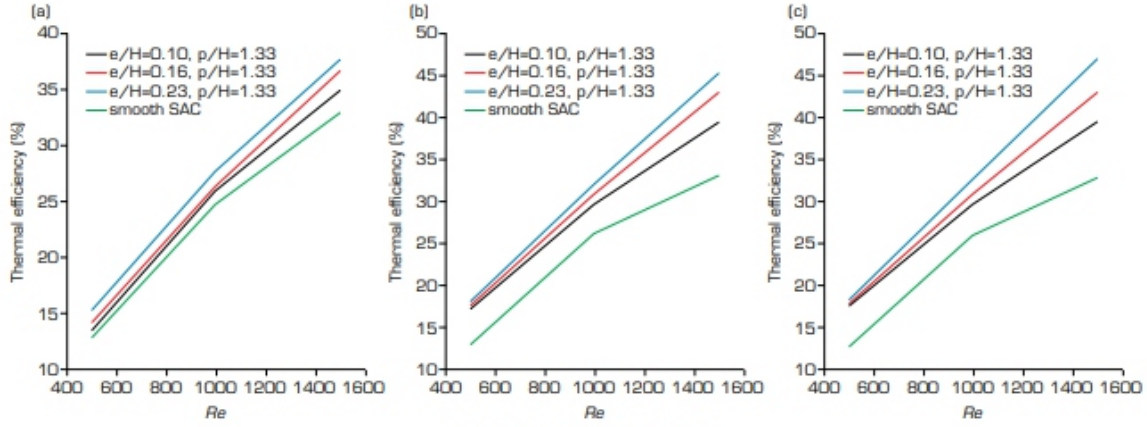


Source: Elaborated by the authors.

**Figure 9.** Variation of average thermal efficiency for smooth SAC and v-corrugation SAC at different values of height and pitch with Reynolds number. (a) (p/H) = 1.33 with different values of (e/H); (b) (p/H) = with different values of (e/H); (c) (p/H) = with different values of (e/H).

## Thermohydraulic Performance Parameter (THPP)

Total performance of SACs, taking into account both an improvement in heat transmission and an increase in friction factor. Variation of THPP with Reynolds number is present in Fig. 10 for various heights (e/H) and pitches (p/H) for corrugated air collector. For a height (e/H) of 0.10, 0.16, and 0.23, the values of THPP ranged from 1.118 to 1.220, 1.079 to 1.161, and 1.058 to 1.157, respectively. In each case, the THPP values rised as the Reynolds number decreased. The results show that the values of THPP increased as the (e/H) decreased. Additionally, these values increased as the pitches (p/H) increased. Therefore, it can be said that for low Re, low (e/H), and higher (p/H), the v -corrugation in absorber plate SAC is more effective. In the range of parameters examined, greatest THPP value is 1.220 for (e/H) of 0.10, and (p/H) of 2, at a Re of 500.

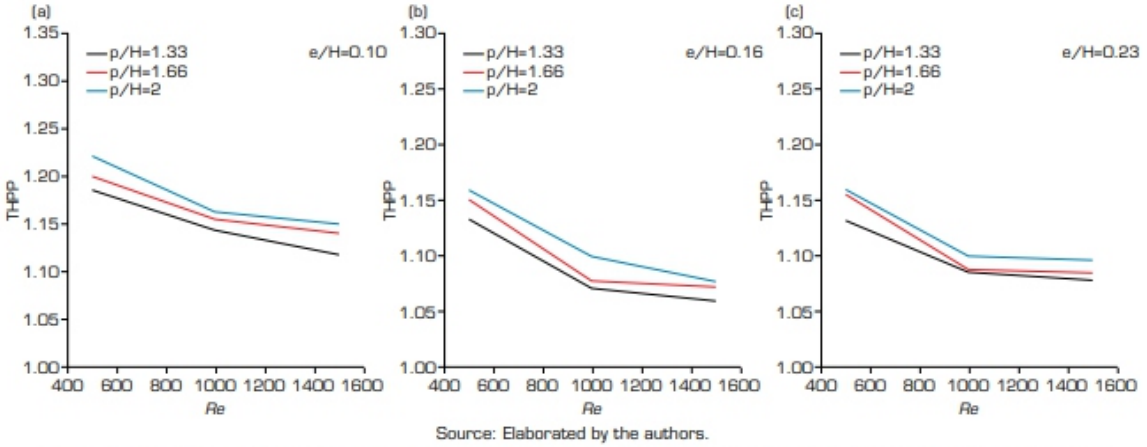


Source: Elaborated by the authors.

**Figure 10.** Variation of THPP for v-corrugation SAC at different values of height and pitch with Reynolds number. (a) (p/H) =1.33 with different values of (e/H); (b) (p/H) = with different values of (e/H); (c) (p/H) = with different values of (e/H).

## CONCLUSIONS

The main findings of this investigation can be summarized as follows:

• The best ways to increase heat transfer rates from heated plates are observed to be v-corrugated roughened surfaces with varying height and pitch.

• The Nu and Ct are significantly influenced by the corrugation's parameters. It is obtained as Re grows, the Ct decreases while Nu increases.

• At a fixed value of (p/H) and Re, the average Nu and Ct rise when the height (e/H) increases, while they reduce as (p/H) rise.

• The highest average outlet temperature is found in the v-absorber SAC, where it is around 61 oC for a (e/H = 0.23 and p/H = 2) as opposed to 53 oC for the smooth absorber SAC.

• The thermal efficiency is at its highest level for a v-corrugation absorber SAC at (e/H = 0.23 and p/H = 2) and it is about 46.7% compared to 33.01% for smooth absorber SAC, which indicate the optimal configuration for a v-corrugation absorber SAC is at (e/H=0.23) and (p/H=2), verify a high performance.

## CONFLICT OF INTEREST

Nothing to declare.

## AUTHORS' CONTRIBUTIONS

Conceptualization: Abed AF; Methodology: Hamad RF; Abed AF; Resources: Hashim NAW; Software: Abed AF; Data curation: Hashim NAW; Formal analysis: Dahham RB; Supervision: Abed AF, Hamad RF; Validation: Dahham RB; Preparation of original draft: Hamad RF; Writing: Abed AF; Proofreading and editing: Hashim NAW

## DATA AVAILABILITY STATEMENT

Data sharing is not applicable.

## FUNDING

Not applicable.

## ACKNOWLEDGEMENTS

Not applicable

## REFERENCES

*1.Aharwal KR, Gandhi BK, Saini JS (2008) Experimental investigation on heat transfer enhancement due to a gap in an inclined continuous rib arrangement in a rectangular duct of solar air heater. Renew Energ 33(4):585-596.*

*2.Amraoui MA, Aliane K (2018) Three-dimensional analysis of air Flow in a flat plate solar collector. Period Polytech Mech Eng 62(2):126-135. https://doi.org/10.3311/PPme.11255*

*3.Chaichan MT, Abass KI, Al-Zubidi DS, Kazem HA (2016) Practical Investigation of Effectiveness of Direct Solar-Powered Air Heater. IJAEMS 2(7):1047-1053.*

*4.Chaube A, Sahoo PK, Solanki SC (2006) Analysis of heat transfer augmentation and flow characteristics due to rib roughness over absorber plate of a solar air heater. Renew Energ 31(3):317-331. https://doi.org/10.1016/j.renene.2005.01.012*

*5.Choi H-U, Choi K-H (2020) CFD Analysis on the Heat Transfer and Fluid Flow of Solar Air Heater having Transverse Triangular Block at the Bottom of Air Duct. Energies 13(5):1099. https://doi.org/10.3390/en13051099*

*6.Darici S, Kilic A (2020) Comparative study on the performances of solar air collectors with trapezoidal corrugated and flat absorber plates. Heat Mass Transfer 56(6):1833-1843. https://doi.org/10.1007/s00231-020-02815-y*

*7.Hakam M, Ichsani D, Suroso C (2016) Numerical investigation of heat transfer and fluid flow characteristic of V-corrugated plate solar air collector with prismatic fin as an extended surface. AIP Conf Proc 1778(1):030009. https://doi.org/10.1063/1.4965743*

*8.Hameed HG, Diabil HAN, Saeed MMA (2021) Performance of A New Model of Air Heating System: Experimental Investigation. J Mech Eng Res Dev 44(5):420-432.*

*9.Hassan HFA (2022) Experimental study and evaluation of single slope solar still combined with parabolic trough using nanofluid (Master's thesis). Najaf: Al-Furat Al-Awsat Technical University. In English. [accessed 2022 May 20]. https://cnj.atu.edu.iq/wp-content/uploads/2022/06/Hawraa-Fadhel-Abd-Hassan-2022-4-25.pdf*

*10.Hedayatizadeh M, Sarhaddi F, Safavinejad A, Ranjbar F, Chaji H (2016) Exergy loss-based efficiency optimization of a doublepass/glazed v-corrugated plate solar air heater. Energy 94:799-810. https://doi.org/10.1016/j.energy.2015.11.046*

*11.Karmare SV, Tikekar AN (2010) Analysis of fluid flow and heat transfer in a rib grit roughened surface solar air heater using CFD. Sol Energy 84(3):409-417. https://doi.org/10.1016/j.solener.2009.12.011*

*12.Kumar A, Gholap A, Gangarde R, Shinde SM, Vyavahare MP, Mete VB, Borude SA (2017) Performance Of Solar Air Heaters With Corrugated Absorber Plate- A CFD Approach. IJIRAS 4(11):76-86.*

*13.Manjunath MS, Karanth KV, Sharma NY (2018) Numerical investigation on heat transfer enhancement of solar air heater using sinusoidal corrugations on absorber plate. Int J Mech 138-139:219-228. https://doi.org/10.1016/j.ijmecsci.2018.01.037NaraghiMH, Blanchard S (2015) Twenty-four-hour simulation of solar chimneys. Energy Build 94:218-226. https://doi.org/10.1016/j.enbuild.2015.03.001*

*14.Promvonge P, Promthaisong P, Skullong S (2022) Heat transfer augmentation in solar heat exchanger duct with louver punched V-baffles. Sol Energy 248:103-120. https://doi.org/10.1016/j.solener.2022.11.009*

*15.Rouissi W, Naili N, Jarray M, Hazami M (2021) CFD Numerical Investigation of a New Solar Flat Air-Collector Having Different Obstacles with Various Configurations and Arrangements. Math Probl Eng 2021:9991808. https://doi.org/10.1155/2021/9991808*

*16.Salih SM, Alsabery AI, Hussein AK, Ismael MA, Ghalambaz M, Hashim I (2023) Melting control of phase change material of semi-cylinders inside a horizontal baffled channel: Convective laminar fluid–structure interaction. J Energy Storage 58:106312. https://doi.org/10.1016/j.est.2022.106312*

*17.Varol Y, Oztop HF (2007) Buoyancy induced heat transfer and fluid flow inside a tilled wavy solar collector. Build Environ 42(5):2062-2071. https://doi.org/10.1016/j.buildenv.2006.03.00*

*18.Winbank WC (1963) Long-wave radiation from clear skies. Q J R Meteorol Soc 89(381):339-348. https://doi.org/10.1002/qj.49708938105*

*19.Yadav AS, Bhagoria JL (2013) Modeling and Simulation of Turbulent Flows through a Solar Air Heater Having Square Sectioned Transverse Rib Roughness on the Absorber Plate. Sci World J 2013:827131. https://doi.org/10.1155/2013/827131*

*20.Zheng W, Zhang H, You S, Fu Y, Zheng X (2017) Thermal performance analysis of a metal corrugated packing solar air collector in cold regions. Appl Energy 203:938-947. https://doi.org/10.1016/j.apenergy.2017.06.0*

# Design & Implementation of an Electric Fixed-wing Hybrid VTOL UAV for Asset Monitoring

**Sarvesh Sonkar1 , Prashant Kumar2 , Yuvaraj Tanjore Puli3 , Riya Catherine George4,* , Deepu Philip5 , Ajoy Kanti Ghosh2**

1.Indian Institute of Technology Kanpur – Design – Kanpur/Uttar Pradesh – India. 2.Indian Institute of Technology Kanpur – Aerospace Engineering – Kanpur/Uttar Pradesh – India. 3.GAIL (India) imited – Noida/Uttar Pradesh – India. 4.Hiroshima University – Civil and Environmental Engineering – Higashi Hiroshima/Hiroshima – Japan. 5.Indian Institute of Technology

## ABSTRACT

*Fixed-wing unmanned aerial vehicles (UAVs) offer the best aerodynamic efficiency required for long-distance or high-endurance applications, albeit their runway requirement for take-off and landing in comparison with quadcopters, helicopters, and flapping-wing UAVs that can perform vertical take-off and landing (VTOL). Integrating a multirotor system with a fixed-wing UAV imparts VTOL capabilities without significantly compromising fixed-wing aerodynamic efficiency, endurance, payload capacity or range. Documented system design approaches to address various challenges of such fusion processes are sparse. This research proposes a holistic approach for designing, prototyping, and testing an electric-powered fixed-wing hybrid VTOL UAV. The proposed system design approach augments the standard aircraft design process with additional steps to integrate VTOL capabilities. Separate fixed-wing and multirotor designs were derived from the frozen mission requirements, which were then fused. The process used simulation for modeling and evaluating alternatives for the hybrid UAV created using standard aircraft design equations. We prototyped and instrumented the final design to validate operational capabilities through test flights. Multiple flight trials identified the ideal combination of Lithium-Polymer (Li-Po) batteries for VTOL (8000mAh) and fixed-wing (14000mAh) modes to meet the endurance and range requirements. The redundant power supplies also increased the survivability chances of the hybrid UAV during failures.*

***Keywords: Hybrid; UAV; VTOL; BLDC; Fuselage; Aircraft design***

## I. INTRODUCTION

UAVs are becoming popular in avenues like aerial photography, surveying, monitoring, border patrol, surveillance, etc. (Sonkar et al. 2020; 2021). Researchers identified applications of UAVs in precision agriculture, package delivery, disaster management, etc., to improve efficiency and commercial viability (Sun et al. 2016; Kumar et al. 2020). Two types of UAV platforms, viz., (i) rotary-wing and (ii) fixed-wing, are famous for such applications (Ebeid et al. 2017; Zhang et al. 2021). Rotary-wing systems possess enhanced maneuverability (Matsumoto et al. 2010), vertical take-off and landing (VTOL) capability, and midair hovering ability during flight (Sonkar et al. 2020). However, their inefficient operational nature severely limits both endurance and range. In contrast, fixed-wing UAVs

*ef*ficiently utilize power, resulting in longer endurance and better flying range (Bauersfeld et al. 2021).

However, their requirement for a runway or catapult launch/arrest system for take-off and landing restricts their operations to locations with such infrastructure. The recent concept of the hybrid UAV capable of VTOL is popular among the research community, while not very popular in real-world applications (McCormick 1999; Stone et al. 2008).

Combining features of both types result in tail-sitter (Lyu et al. 2017), tilt-rotor (Matsumoto et al. 2010), and hybrid VTOL UAVs (Wan et al. 2019). A tail-sitter UAV does its vertical climb on the empennage and then tilts the entire airframe horizontally for its level flight, accomplishing both tail-sitting and level flying using the same engines (Kubo and Suzuki 2008). But, the tilt-rotor UAVs only tilt their propulsion systems (motors) vertically and horizontally to achieve both take-off and forward flight, respectively (Bauersfeld et al. 2021). This research proposes an augmented, holistic approach based on the standard aircraft design process to design a hybrid VTOL UAV as a fusion of rotary and fixed-wing systems. This iterative process allows quickly processing of design alternatives and converges them to a viable design that can be flight tested.

Recently, electric propulsion applications for various transportation modes have increased significantly (Zong et al.2021). Electric-powered fixed-wing UAV systems (Gur and Rosen 2009; Roskam 1985b) are becoming increasingly popular, with specific models being mass-produced. Small and medium-sized electric UAVs are gaining market popularity (Lyu et al. 2017), albeit having a much shorter range and endurance in comparison with the internal combustion engines (ICEs) propelled models (Ge et al. 2021; Oh et al. 2021). Existing technologies in Lithium-Ion (Li-Ion) and Lithium-Polymer (Li-Po) batteries allow energy densities up to 300-500 watt-hours/kg (Wh/kg) (Girishkumar et al. 2010). However, UAVs with ICEs burning aviation fuel offer more than 1400 Wh/kg (Cwojdziński and Adamski 2014). While the theoretical limit of 370 Wh/kg for Li-Ion batteries is rapidly approaching (Li et al. 2017), two UAVs, viz., (i) "Zephyr" and (ii) "ALTI" demonstrated long endurances with energy densities between 350-380 Wh/kg (Rapinett 2009). Lithium–Sulfur (Li-S) and Lithium–Oxygen (Li-O) batteries offer futuristic promise with their theoretical energy densities of ~2570 and ~3500 Wh/kg,respectively (Luongo et al. 2009).

The electric motor is an essential component of electric propulsion. Lightweight brushless direct current (BLDC) electric motors under 360 kW are now available in the market (Jing et al. 2022). In the near future, small and medium electric UAVs will be able to compete with traditional ICE-powered UAVs (Xie et al. 2022). Simultaneously, multi-copter UAVs are gaining popularity due to maneuverability, controllability, and VTOL characteristics (Prouty 1995; Bhandari et al. 2017; Boon et al. 2017).

Multi-copter UAVs are easily manufacturable, with major sub-systems being a chassis, control board (autopilots), direct drive motors, batteries, and propellers. Simple alteration of the motor voltages can control the propeller rotation speed (RPM) (Çakici and Leblebicioğlu 2016). However, the high energy consumption of multi-copters results in shorter operational times. Alternatively, fixed-wing systems possess higher cruising efficiency (Garcia-Nieto et al. 2019), which translates to increased endurance and payload capacity.

The desire to combine the advantages of the fixed-wing and multi-copter systems resulted in the development of the hybrid VTOL system depicted in Fig. 1, which integrated the multi-copter propulsion into a conventional fixed-wing system. M1, M2, M3, and M4, in Fig. 1, represent the four vertical motors of the hybrid VTOL UAV. Such hybrid VTOL systems are ideal for aerial mapping, surveillance, and precise delivery applications. For example, small hand-launched fixed-wing UAVs such as PrecisionHawk Lancaster, senseFly eBee, and medium-sized catapult-launched UAVs like Penguin BE, currently dominate the aerial mapping and surveillance industry. We conducted multiple flight tests using the prototyped design of the final configuration to quantify range, endurance, and fail-safes. The payload integration occurred after such test flights established the design's robustness. Sonkar et al. (2022) have published the results of such experimental flights using the payload-integrated prototype

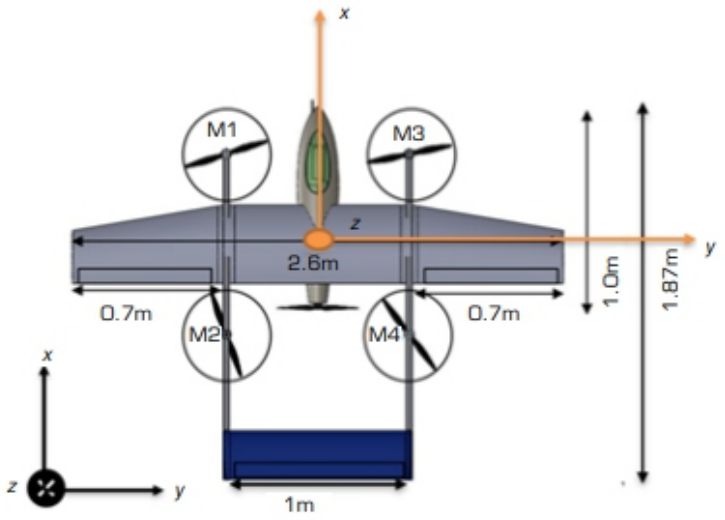


Fixed-wing aircraft design relies heavily on methods that calculate the size, mass, and power requirements, where numerous well-known scaling techniques exist. Raymer (2018) introduced the first weight estimation method using the mission profile and a set of empirical equations for the ICE-powered aircraft. Earlier, McCormick (1999) created recommendations for the UAV mass breakdown and determined the battery mass percentage required for fixed-wing cruise flight of an electric fixed-wing UAV. Then, Bhandari et al. (2017) provided an integrated approach to assess the size of crewed electric fixed-wing aircraft. Zong et al.(2021) proposed a system for sizing heavy ICE-powered VTOL aircraft with maximum take-off weights (MTOW) of up to 27.5 tons. The designer's experience and suggestions from manufacturers primarily determine the propeller-motor combination. Recent research interests in commercial hybrid VTOL UAVs focus more on the control logic (Saeed et al. 2018). Researchers have reported a commercial hybrid VTOL UAV for medical applications with an MTOW of 25kg using ICE propulsion (Goetzendorf-Grabowski et al. 2021), which provided the impetus for the proposed design process of this research. This research also offers additional design process innovations like empennage modifications, boom-mount vertical propulsion, lightweight manufacturing process, etc.

This research proposes an alternative design process for fixed-wing hybrid VTOL UAVs with electric propulsion. Creating separate and different designs for the fixed-wing and rotary-wing systems based on the mission and performance requirements becomes the preliminary step of our process, as explained in the airframe design section. Then, the selection and fusion of these designs occurred as the next step that created multiple realizations of the electric fixed-wing hybrid VTOL UAV. After selecting design(s) that fulfill the basic functionality requirements, design sizing of the wing, fuselage, tail, and control

surfaces happened as part of the next to attain optimal performance against specific choices of various components of UAV sub-systems. The designed hybrid UAV has five sub-systems, viz., (i) airframe (multirotor and fixed-wing), (ii) propulsion, (iii) control, (iv) communications, and (v) payload (camera and gas sensor). Specific component choices in each sub-system influence the overall system performance, requiring iterative re-design. The intended application of the designed fixed-wing hybrid VTOL UAV was natural gas pipeline monitoring along with onboard leakage detection. Our work also documents the evaluation of the configuration's efficiency, validation of the selected sizing/resizing technique, and testing of the control algorithms. The following sections first discuss the preliminary design, followed by the actual design of the experimental hybrid UAV. The final sections detail the testing and performance benchmarking.

**Airframe design**

This section describes the intended mission profile, which formed the foundation for designing the fixed-wing hybrid VTOL UAV. The intended usage of the UAV is monitoring natural gas pipelines with additional capability of leakage detection. Major subsections are mission requirements, wing, tail, fuselage designs and the VTOL section.

**Mission requirements**

The design space for the fixed-wing hybrid VTOL UAVs is a continuum created to conduct autonomous surveillance, asset monitoring and leakage detection of underground natural gas pipelines. The need to take off and land along the underground gas pipeline without runway infrastructure necessitates VTOL capability. Further, long pipeline stretches warrant extended operational ranges, which translates to extended endurance to cover such distances. A fixed-wing system's efficiency helps fulfill such endurance and range requirements. Thus, the categories identified from the mission requirements include weight, size, flying altitude, survivability, the need to combine the fixed-wing and rotary-wing systems, etc. The mission profile of the hybrid fixed-wing VTOL UAV has five main flight segments viz., (i) vertical take-off, (ii) forward transition (switch to quad mode from fixed-wing mode), (iii) cruise, climb, and loiter, (iv) back transition (switch from fixed-wing mode to quad mode), and (v) vertical landing as depicted in Fig. 2. Table 1 summarizes the initial design parameters derived from the mission requirements.

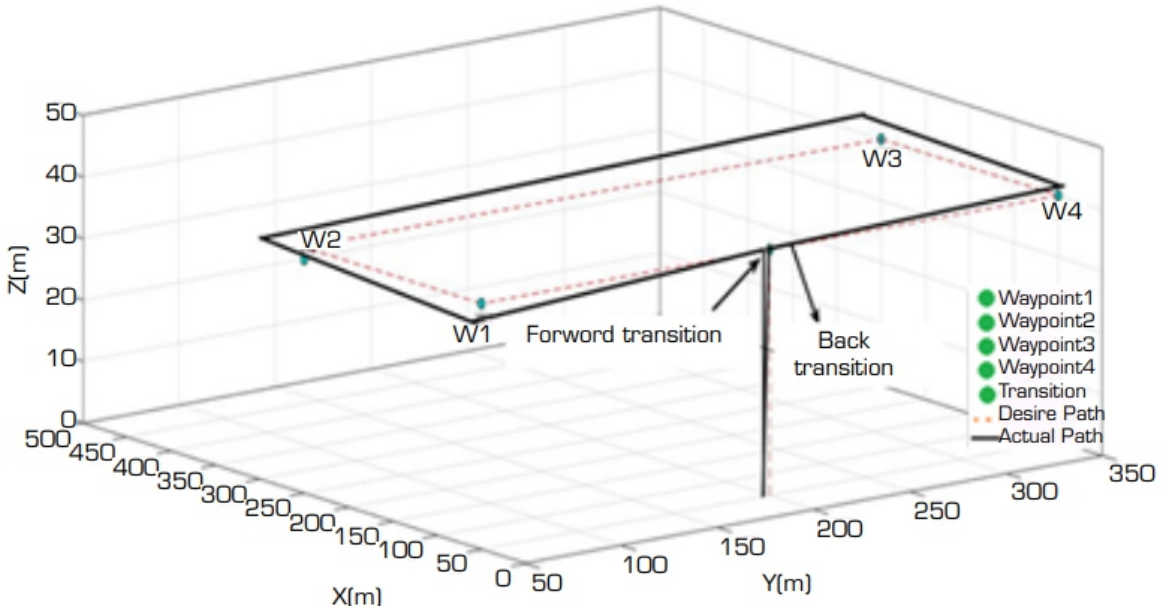


Source: Elaborated by the authors.

**Figure 2**. Mission Profile of Hybrid VTOL UAV.

**Table 1.** Hybrid UAV design parameters derived from the mission requirements

| **Maximum Take-Off Weight (MTOW)** | **< 12 kg** |
|---|---|
| Payload capacity | <1.8 kg |
| Runway length for the take-off | 0 m |
| Rate of ascend (multirotor mode) | 2.5 m/s |
| Rate of descend (multirotor mode) | 3.5 m/s |
| Climb rate in the fixed-wing mode | >2.5 m/s at Mean Sea Level (MSL) |
| Operational altitude (from take-off point) | 200 m Above Ground Level (AGL) |
| Endurance | >45 min |
| Range | >20 km |
| Propulsion System | Electric Motors |

Source: Elaborated by the authors.

## Preliminary Design & Sizing

The preliminary design process focused on broadly identifying the weight, shape, and propulsion system from the mission requirements. Further, fine-tuning of these parameters using additional information about other sub-systems/components, including various choices of BLDC motors, batteries, etc., helped finalize designs. Figure 3 illustrates the analytical process of the fixed-wing system design phase, having three sub-phases, viz., (i) configuration selection, (ii) conceptual design, and (iii) development and validation of the conceptual design. Figure 3 also depicts the iterative

iterative refinements made to the conceptual design between phases (ii) and (iii).

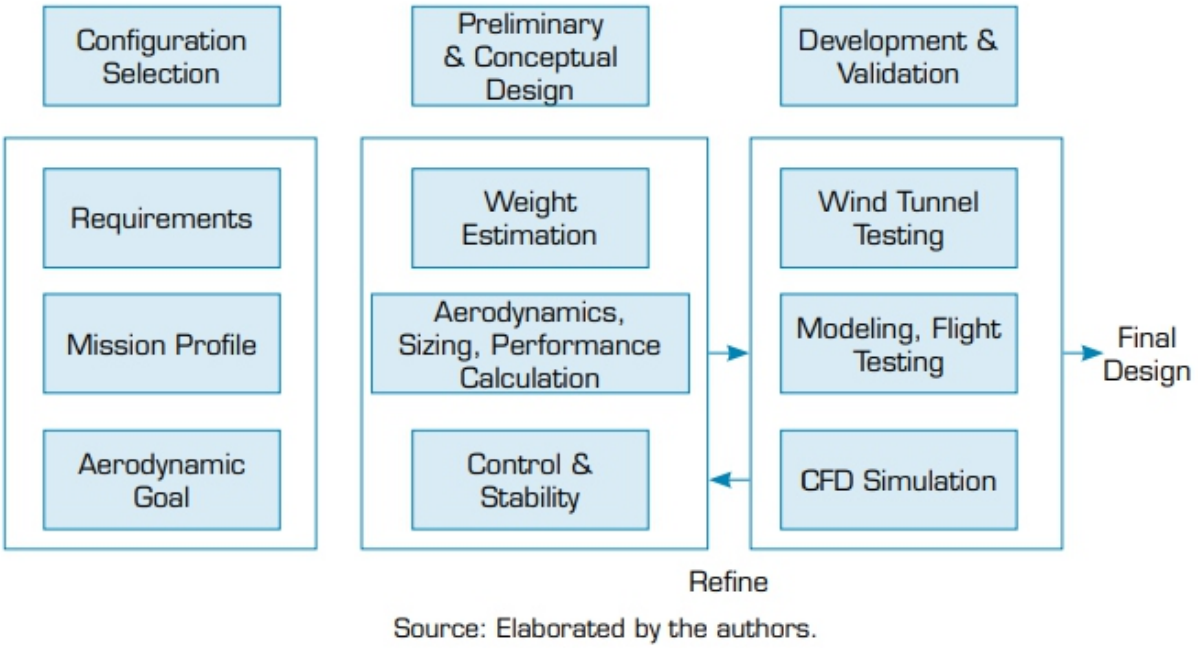


**Figure 3.** Design process of the fixed-wing hybrid VTOL UAV

Identifying specific performance and mission requirements during phase (i) initiated the design process. We assumed that components viz., motors, propellers, and batteries that match the computed specifications are available in the market. First, we estimated the propulsion system's initial geometry, mass, thrust parameters, etc., followed by a numerical investigation similar to that of Oktay and Eraslan (2021) of the multirotor VTOL UAV propellers to determine the impact of airspeed and rotational speed on thrust coefficient. All these facilitated the selection of the actual models of BLDC motors, composite propellers, and Li-Po batteries for the hybrid UAV. Continuous updation of the hybrid UAV's MTOW occurred according to such choices of sub-systems.

## WING DESIGN

Wing primarily generates the required lift for a fixed-wing aircraft along with drag and moment (nose down generally) simultaneously. Hence, factors such as performance requirements, stability, ease of control, manufacturability, system costs, flight safety, etc., are essential for wing design. Major performance requirements of the hybrid UAV include stall speed, maximum speed, range, and endurance. Körpe et al. (2019) presented the turbulence model to perform a numerical analysis of the impact of the dimensionless wall distance on the aerodynamic coefficient of an aerofoil. Next, longitudinal and lateral directional stability constitute the major stability requirements. Other parameters influencing the wing design process include wing area, airfoil selection, aspect ratio, taper ratio, tip chord, sweep angle, dihedral angle, incidence angle, aileron sizing, servo mounting position, etc. Size and weight constraints mainly limit the minimum wing size.

We considered four different wing designs viz and after comparisons, we reached the following conclusions:

• Rectangular wing generates the lightest wing loading for the given constraints, resulting in the lowest lift coefficient (CL) value for cruise flight. Further, the lift distribution pattern and substantial tip losses ruled out this design.
• Tapered wing provides better lift distribution than the rectangular wing. But, larger wing loading coupled with a higher CLrequirement for cruise makes this design less preferred.
• Elliptical wing offers the best lift distribution and negligible wing tip losses. However, this design also suffers from high wing loading CL requirements and added manufacturing difficulty.
• Semi-tapered wing has similar lift distribution as that of a tapered wing while eliminating the need for wing tip modification to reduce tip losses. The wing loading is less than both tapered and elliptical wings, as the CL required for the cruise is also less.

Though the research suggests that an elliptical wing offers better lift distribution with minimal drag, its manufacturing is costly and time-consuming. Further, the Reynolds Number towards the elliptical wing tip becomes relatively small, causing significant deviations in its lift estimations. Choosing the semi-tapered wing shown in Fig. 4, it resulted in a more straightforward design with better aerodynamic and structural advantages, as evaluated using the XFLR5 software. Further, the semi-tapered wing is relatively easy to fabricate and provides good lift distribution.


Source: Elaborated by the authors.

**Figure 4**. Wing geometry of the fixed-wing system in XFLR 5

XFLR5 is a design and analysis tool for wing, tail, and airfoils at low or high Reynolds numbers (Dwivedi et al. 2020). Figure 5 depicts the resulting elliptical lift distribution curves after using the Horseshoe Vortex method for estimating lift in XFLR5. The final wing design resulted in a span of 2.6m, wing area of 0.9m2, mean aerodynamic chord of 0.35m, and cruise speed of 17m/s. We conclude from Fig. 5 that the lift is maximum at the root chord and minimum at the tip chord of the wing. Specific attention during design avoided the over-tapering of the wing, thereby eliminating its associated complications. A strong taper of the wing causes the local lift coefficient, CL(wing), to have a maximum value near the root (Fig. 5), creating the adverse possibility of tip stall during flight. Moreover, it also causes small chords Reynolds Number near the tip, thereby reducing the maximum achievable CL of the wing. Wing loading is the ratio of the aircraft's MTOW to its wing area, which is a critical parameter of the fixed-wing aircraft design.

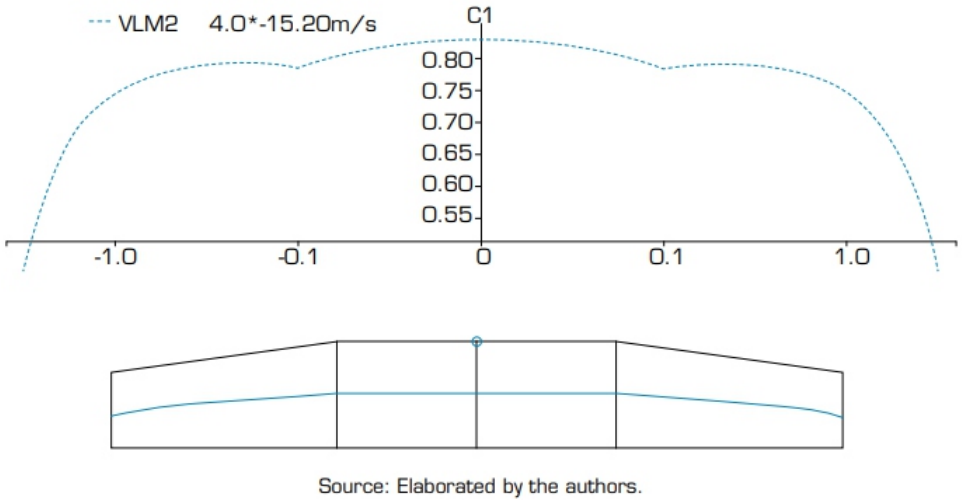


Source: Elaborated by the authors.

**Figure 5.** Lift distribution along the wing estimated using XFLR5.

Figure 6a shows the wing loading while operating at the maximum lift coefficient (C(LMax) ) for various altitudes, viz., 100, 300, and 500 meters. Factors like the UAV wing's size, shape, and attachment angle on the fuselage determine its take-off and landing performance, stall speed, and maneuverability. Greater wing loading helps to maintain smaller wing sizes with respect to the aircraft's mass. If all other factors remain constant, the UAV with smaller wings will have a lower stall speed (making it quicker at cruising speed) than one with larger wings. In addition, UAVs with greater wing loading will be more stable in steady flight than those with lower wing loading.The mission requirements mandate a low cruise speed (about 16-18 m/s), thereby freezing the maximum wing loading for a given stall speed (estimated around 18-20 kg/m2), and determining the wing sizing. Also, researchers advise maintaining wing loading that realizes nearly 20% structural safety (Roskam 1985b). Figure 6b depicts the V-n diagram that plots the load factor against the velocity. Maintaining lower loiter or cruise speeds are generally advised to lower the dynamic pressure, thus generating lesser loads on the structure. Lower wing loading helps achieve lower stall velocity, resulting in lower cruise speed. We can achieve lower wing loading by reducing the weight for a given wing area, which in turn results in a load lower than the usual on the wing during maneuver (L = nW, where n is the load factor).

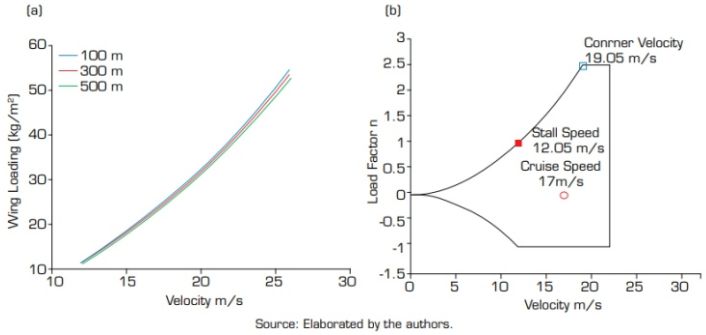


Source: Elaborated by the authors.

**Figure 6.** (a) Wing loading vs. velocity for fixed-wing design at (C(Lmax)

The wing incidence angle is the pitch angle of the wing to the fuselage. In the case of an untwisted wing, it is simply the angle between the airfoil chord line and the fuselage reference line. Usually, minimization of drag during cruise flight drives the choices of wing incidence angle. This implies that when the wing is at the desired angle of attack (AOA) for the chosen design condition, the fuselage is at the AOA that minimizes the total drag.

## TAIL GEOMETRY AND SIZING

The tail provides stability to the UAV. Zero-loaded tails are usually preferred so that the lift coefficient for the designed configuration is zero, thereby keeping the induced drag zero. Numerous tail configurations exist identical to that of the manned aircraft that can have single or multiple attachment points. Before finalizing the tail configuration, we compared the advantages and disadvantages of major tail designs reported in the literature, like U, inverted U, V, inverted V, T, inverted T, H, etc.

Both U and inverted U tails possess the same number of surfaces, viz., two vertical and one horizontal. Further, both tail designs do not obstruct the wing downwash, prop wash, wakes, and vortices. However, they suffer from a destabilizing effect at higher AOAs as aerodynamic loads on the horizontal tail get transferred to the vertical tails and booms. Additional strengthening of the vertical tails solves this issue but increases the total weight. H-tail design has one horizontal surface between two vertical tails, combining the advantages while eliminating the disadvantages of both U and inverted U tails. However, careful determination of the relative location of the horizontal tail is necessary to negate any deep stall, thereby making the design process more complex. The added weight due to additional strengthening further makes this design costly. Finally, both V and inverted V-tails have only two slanted surfaces that realize the same functions as the elevator and rudder of a conventional tail configuration, thereby reducing the drag and weight. Conversely, its control system is more complex due to the simultaneous occurrence of elevator and rudder components during various maneuvers compared with other configurations.

We chose the inverted U-tail design with a pusher configuration for the fixed-wing UAV design, having a twin-boom connection to the fuselage. Figure 7 depicts the tail design, including the tiny tappers on the vertical control surfaces. Both horizontal and vertical tail sections of Table 3 summarize the principal design parameters of both surfaces. The simplicity of this design resulted in better manufacturability, maintainability, and overall efficiency. Further, the horizontal tail tends to provide more drag and stabilizing effects at high angles of attack. The structural heaviness and its associated marginal costs vastly outnumbered the benefits of this design.

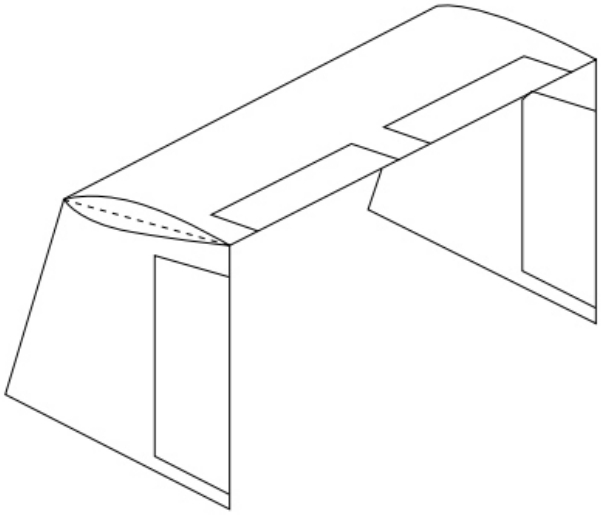

Source: Elaborated by the authors.

## FUSELAGE DESIGN

Fuselage design is a complicated process involving several factors like payload capacity, avionics, battery sizes, propulsion, and other parameters depending upon the UAV's applications. Hence, we used the guidelines of Roskam (1985a) and Nelson (1989) to analyze the design parameters. We chose a simple symmetric fuselage geometry and analyzed it to obtain a rough estimate of the pitching moment due to the fuselage at an AOA *(C(m))f* and pitching moment with zero AOA *(C(mo))f*. Throughout the design iterations, Eqs. 1 and 2 facilitated the revision of fuselage geometries and the corresponding values of *(C(mα))f* and *(C(mo)f*respectively (Roskam 1985b). Figure 8 indicates the oval shape of the UAV's fuselage, which also integrates two square hollow tubes to facilitate the attachment of the tail booms. Table 2 compiles all major fuselage specifications of the hybrid UAV. Since the intended application of the UAV is surveillance, reconnaissance, and asset monitoring, the primary payload consists of a gas sensor and a gimbal camera. These payload considerations also determined the access points location along with the width and length of the fuselage.

$$\left(C_{m_\alpha}\right)_f = \frac{(K_2 - K_1)}{36.5S\underline{c}} \sum_{x=0}^{x=lf} \quad W^2 f\left(\alpha_{0w} + i_f\right)\Delta x \tag{1}$$

$$C_{mof} = \frac{1}{36.5S\underline{c}} \sum_{x=0}^{x=lf} \quad \frac{W^2 f(\partial \epsilon_u)}{\partial \alpha}\Delta x \tag{2}$$

Where:S= wing reference area; c_ = wing mean aerodybamic; wf = average widith of fuselage section; Δx = length of fuselage increment; Aow = wing zero lift angle relative to fuselage ref. line in degrees (−4°); if = incidence of the fuselage camber line relative to the fuselage reference line at the entre of each fuselage increment; K2 – K1 is the correction factor used for designing the overall shape of a streamlined body (fixed-wing hybrid VTOL UAV); (δευ)/δ = change in local flow angle with angle of

attack.

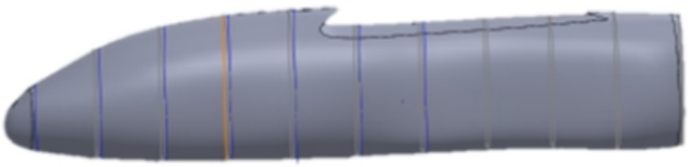

Source: Elaborated by the authors.

**Figure 8**. 3D Fuselage Design.

**Table 2.** Fuselage Specifications

| Parameter | Symbol | Values |
|---|---|---|
| Length of fixed-wing UAV(m) | $L_0$ | 1.78m |
| Length of the cockpit(m) | $L_{cockpit}$ | 1.0m |
| Max width of the cockpit(m) | $W_{cockpit}$ | 0.15m |
| Max width of the tail boom(m) | $W_{boom}$ | 0.025m |
| Fuselage depth | $d$ | 0.17m |
| Fuselage side area($m^2$) | $S_{f_u}$ | 0.1438sq.m |
| Fuselage pitching moment Coeff. at $\alpha = 0$ | $(C_{m_o})_f$ | -0.0178 |

Source: Elaborated by the authors.

## DESIGN SUMMARY AND CHARACTERISTICS

This section summarizes the complete UAV geometry by compiling all pertinent information from the previous sections. Standard values published in textbooks and documents helped in sizing the control surfaces. The validation and verification of the geometry occurred through necessary parameter estimations, and stability and control derivatives while making iterative design changes. Fixed-wing systems efficiently recover from stall during forward flight by lowering the nose to gain airspeed. The presence of the independent quadcopter VTOL system provides an additional safety net.

Further, the separate VTOL system can slow the fixed-wing flight to hover, providing an added benefit. Table 3 summarizes the fixed-wing hybrid VTOL UAVs' primary design and control parameters in five parts. The first part tabulates the major missionrelated and physical parameters, while the second details the wing-related parameters. The third and fourth parts of Table 3 contain the horizontal and vertical tail parameters, respectively. The last part of Table 3 summarizes the parameters for the independent rotary-wing VTOL section.

**Table 3**. Full Parameter List of the Fixed-wing Hybrid VTOL UAV

| Parameter | Hybrid UAV |
|---|---|
| Total Weight of Aircraft (kg) | 12 |
| Cruise Velocity of Aircraft (m/s) | 17~18 |
| Ambient Air Density (kg/m$^3$) | 1.2 |
| Position of Centre of Mass w.r.t. wing L.E. (m) | 0.131 |
| Position of Neutral point w.r.t. wing L.E. (m) | 0.205 |
| Wingspan (m) | 2.6 |
| Length of wing root chord (m) | 0.38 |
| Length of wing tip chord (m) | 0.27 |
| **Wing** | |
| Wing Airfoil | E-214 |
| Wing Setting angle (deg.) | 0 |
| Sweep of wing mid-chord points (deg.) | 0 |

Continue…

**Table 3.** Continuation.

| Parameter | Hybrid UAV |
|---|---|
| Lift at zero angle of attack | 0.3260 |
| Setting angle of Wing | 0 |
| Aileron span (m) | 0.8 |
| Aileron chord (m) | 0.085 |
| **Horizontal Tail** | |
| Horizontal Stabilizer Span (m) | 1 |
| Length of horizontal stabilizer root chord (m) | 0.18 |
| Length of horizontal stabilizer tip chord (m) | 0.18 |
| Horizontal Stabilizer airfoil | NACA0012 |
| Tail setting angle (deg.) | ≈-2 |
| Length of the horizontal tail arm (m) | 1.09 |
| Horizontal tail volume efficiency | 0.6 |
| Elevator span (m) | 0.92 |
| Elevator chord (m) | 0.06 |

| Vertical Tail | |
|---|---|
| Vertical Stabilizer Span (m) | 0.2 |
| Length of vertical stabilizer root chord (m) | 0.22 |
| Length of vertical stabilizer tip chord (m) | 0.18 |
| Vertical Stabilizer airfoil | NACA0012 |
| Sectional lift curve slope of vertical stabilizer airfoil | 5.9689 |
| Rudder span (m) | 0.16 |
| Rudder chord (m) | 0.06 |
| Length of vertical tail arm (m) | 1.06 |
| Vertical tail volume efficiency | ≈0.04 |
| **Vertical Thrusters** | |
| M1, M2, M3, M4 Weights (kg) | 1.2 |
| Distance between M1, M2 and M3, M4(axial) (m) | 0.94 |
| Distance between M1, M2 and M3, M4(Parallel) (m) | 1 |

Source: Elaborated by the authors.

Now, we document the performance testing of the prototyped fixed-wing hybrid VTOL UAV. Table 4 details the exact physical parameters of the prototype having a wing area of 0.88 m2, a wingspan of 2.6m, and a mean aerodynamic chord of 0.34m. Figure 1 indicates that the x-axis is in the forward direction along the nose, the y-axis is along the wing, and the z-axis is facing downwards. *Ixx, Iyy, Izz & Ixz.* Together, they represent the moment of inertia values of the system about the x, y, and z-axis. Calculating the moment of inertia utilized the 3D CAD model of the fixed-wing hybrid VTOL UAV. The values of *Ixy, Iyz* were negligible and, hence, taken as zero.

| Parameter | Value |
|---|---|
| Mass | 12 Kg |
| MAC | 0.34 m |
| Wingspan | 2.6 m |
| Area | 0.87 $m^2$ |
| $I_{xx}$ | 3.551 $kgm^2$ |
| $I_{yy}$ | 4.4221 $kgm^2$ |
| $I_{zz}$ | 7.4841 $kgm^2$ |
| $I_{xz}$ | 0.1274 $kgm^2$ |

Source: Elaborated by the authors.

Four main performance parameters measured from test flights include (i) trim velocity, (ii) trim AOA, (iii) aerodynamic efficiency (L/D), and (iv) elevator trim (δε). The estimation of range and required power depends on these parameters. Figure 9 compares the performance plots of the fixed-wing hybrid

VTOL UAV prototype. As observed from Fig. 9a, the trim AOA is approximately 4.5 degrees, and the lift coefficient at the trim CLtrim. The condition is 0.6877 from Fig. 9b. Further, Fig. 9c and d provide the aerodynamic efficiency and power required at trim conditions. Figure 9e depicts the elevator needed to trim the UAV, which indicates the required elevator values at the UAV's center of gravity (CoG) to determine elevator deflection limits. The CoG locations of elevator deflections are about the wing's leading edge reference line shown in Fig. 4. Thus, Fig. 9e allows the checking of the elevator limits against CoG location for different airspeeds. Since the elevator can deflect between +6 to -25 degrees in either direction from the trim conditions, Fig. 9e also helps to determine the forward and backward limits of CoG. Figure 9f plots the relation between the pitching moment (Cm) and the lift coefficient (CL) for different elevator deflections at Xcg = 0.131m and neutral point Xnp = 0.205m, as reported in Table 3.

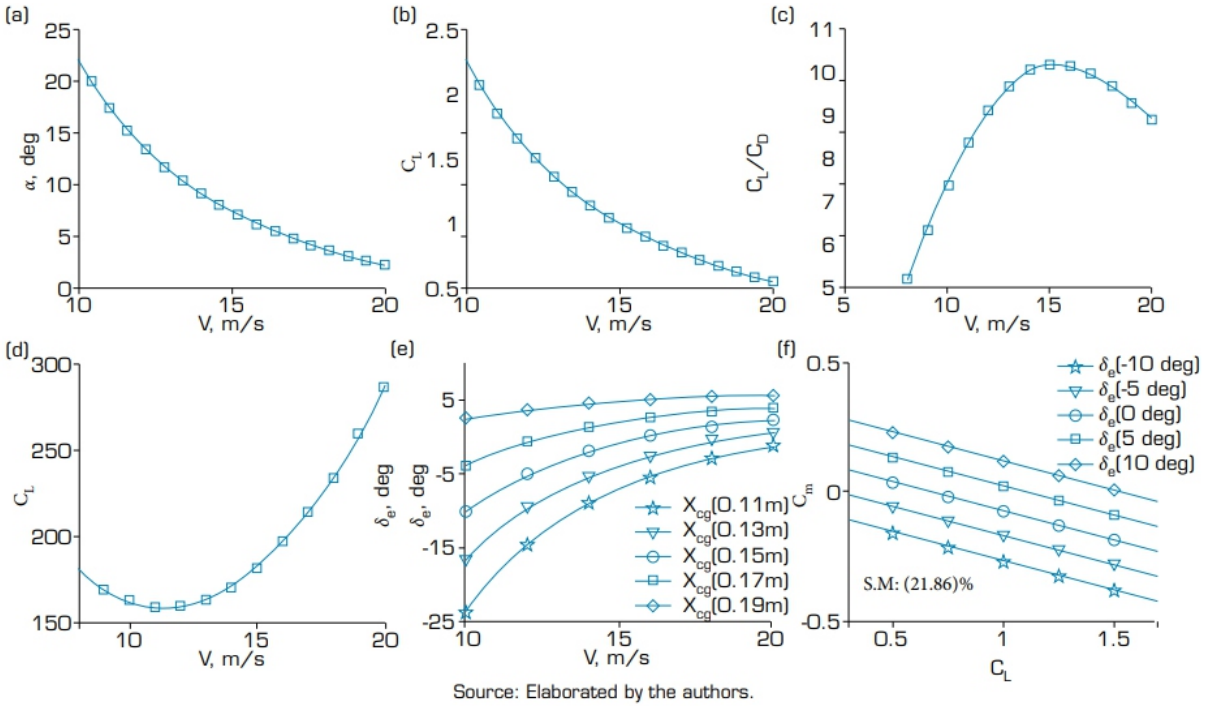

Source: Elaborated by the authors.

**Figure 9**. performance plots for VTOL UAV (a) angle of attack α (b) Lift coefficient (CL) (c) Aerodynamic efficiency(CL/CD) (d) Power Required (PR) (e) Elevator required (δε)versus velocity with CoG variation(f) Pitching moment versus lift coefficient with elevator variation.

Table 5 compiles the prototype's multiple test flights with various Li-Po battery combinations. The second and third columns of Table 5 provide the VTOL and fixed-wing endurance in minutes, respectively, for a specific Li-Po battery combination. The information contained within curly braces in the second and third columns identifies the number of cells (resultant voltage) and energy stored in the particular battery. The fourth column combines the VTOL and fixed-wing flight times, while the last column details the intended application of the UAV configuration. Flight tests eight and nine suggested

d that similar total endurance is possible with a 40% lighter VTOL battery (8,000 mAh) while keeping the same 14,000 mAh battery for the fixed-wing flight.

**Table 5.** Flight times and endurance with different combinations of Li-Po Battery.

| Test Flight | Rotary-wing VTOL endurance for different battery options | Fixed-wing flight-time for different battery options | Total flight time of the hybrid VTOL UAV | Application |
|---|---|---|---|---|
| 1 | (5.25min), {2x6S,5500mAh} | (17min), {6S,6000mAh} | 22.5min | Surveillance, encroachment detection |
| 2 | (6min), {2x6S,6000mAh} | (22min), {6S,8000mAh} | 28min | Surveillance, encroachment detection |
| 3 | (8.2min), {2x6S,8000mAh} | (33min), {6S,10000mAh} | 41.2min | Surveillance, gas-leak detection |
| 4 | (9.3min), {2x6S,9000mAh} | (28min), {6S,9000mAh} | 41.2min | Mapping, encroachment detection |
| 5 | (10.4min), {2x6S,10000mAh} | (28min), {6S,9000mAh} | 37.3min | Mapping |
| 6 | (6min), {2x6S,6000mAh} | (33min), {6S,10000mAh} | 39min | Surveillance, gas-leak detection |
| 7 | (6min), {2x6S,6000mAh} | (53min), {6S,14000mAh} | 58min | Surveillance, gas-leak detection |
| 8 | (8.2min), {2x6S,8000mAh} | (53min), {6S,14000mAh} | 61.2min | Surveillance, gas-leak detection |
| 9 | (10.4min), {2x6S,10000mAh} | (53min), {6S,14000mAh} | 63.4min | Surveillance, gas-leak detection |

Figure 10a illustrates the mission plan displayed on the ground control station (GCS), including two loiters during the flight test. The flight plan consistently subjected the hybrid UAV prototype to various maneuvers along with shorter duration level flights, estimating a reasonably worst-case endurance. It also facilitated the stress test of the control surfaces. Next, Fig. 10b captures the flight of the hybrid UAV high-density foam (HDF) prototype in the VTOL mode.

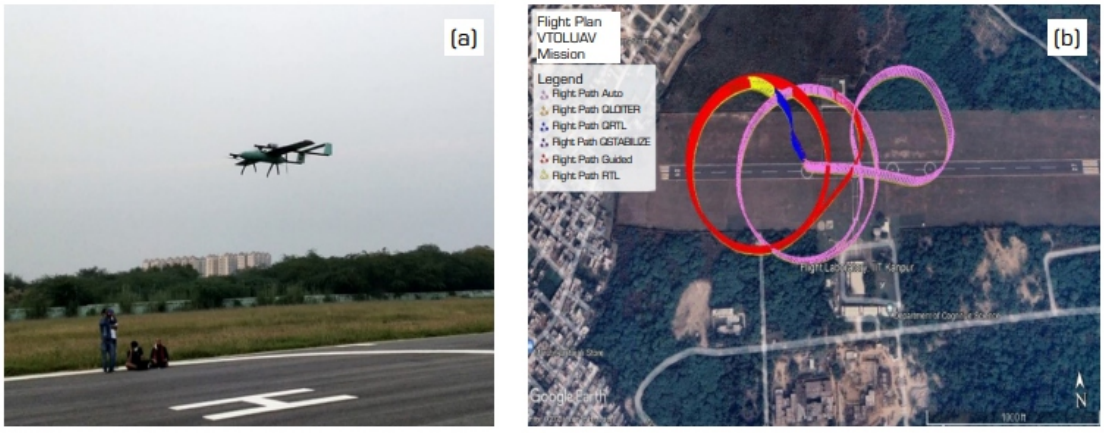


Source: Elaborated by the authors.

**Figure 10.** Flight testing (a) Mission plan from the GCS (b) Actual VTOL flight of the HDF prototype.

## CONCLUSION

This research documents the analytical design, analysis, prototyping, and performance flight testing of a fixed-wing hybrid VTOL UAV with four vertical thrusters (rotary-wing) and one pusher (fixed-wing) propulsion. This research was motivated by the existing lacuna in design approaches for hybrid UAVs that integrate fixed-wing and quadcopter (rotary wing) systems. First, we iteratively determined the hybrid UAV's overall geometry and aerodynamic design for the desired speed and endurance. The entire airframe has three parts, viz., (i) wing, (ii) tail, and (iii) fuselage. Wing design focused on lift distribution and wing loading analysis. Next, we documented the selection approach of the inverted 'U' tail geometry. Finally, standard design equations facilitated the fuselage design to carry specialized payloads. Table 3 summarizes the final design parameters of the resultant fixed-wing hybrid VTOL UAV. Then, we prototyped the fixed-wing hybrid VTOL UAV using HDF, which got instrumented with autopilot, batteries, propulsion units, communication, and payloads. Multiple test flights of the prototyped UAV allowed us to quantify the actual endurance, airspeed, and mission capabilities for different battery combinations, thereby evaluating the design's performance. The combination of an 8,000 mAh battery for VTOL and a 14,000 mAh battery for cruise delivered the desired endurance of 60 minutes with sufficient power remaining in both batteries. Thus, the proposed approach provides a simpler alternative for the quick design and development of a fixed-wing hybrid UAV with VTOL capabilities.

## CONFLICT OF INTEREST

There is no conflict of interest.

## AUTHORS' CONTRIBUTION

Conceptualization: Sonkar S; Kumar P; Ghosh AK; Philip D; Puli YT; Methodology: Sonkar S; Kumar P; Ghosh AK; Software: Sonkar S; Kumar P; Validation: Sonkar S; Kumar P; Formal analysis: Sonkar S; Kumar P; Investigation: Sonkar S; Kumar P; Philip D; Resources: Sonkar S; Kumar P; Philip D; Puli YT; Data Curation: Sonkar S; Kumar P; Philip D; Visualization: Sonkar S; Kumar P; Philip D; Supervision: Philip D; Ghosh AK; George RC; Project administration: Philip D; Funding acquisition: Philip D; Writing – Original Draft: Sonkar S; Writing – Review & Editing: Philip D; George RC.

## DATA AVAILABILITY STATEMENT

Some or all data used in this study are owned by the funding agency and may only be provided with restrictions.

## FUNDING

This project was funded by Gas Authority of India Limited.

**ACKNOWLEDGEMENTS**

Not applicable

**REFERENCES**

*1.Bauersfeld L, Spannagl L, Ducard GJJ, Onder CH (2021) MPC Flight Control for a Tilt-Rotor VTOL Aircraft. IEEE Trans Aerosp Electron Syst 57(4):2395-2409. https://doi.org/10.1109/TAES.2021.3061819*

*2.Bhandari S, Navarro P, Ruiz A (2017) Flight Testing, Data Collection, and System Identification of a Multicopter UAV. Paper presented AIAA Modeling and Simulation Technologies Conference. AIAA Sci Tech Forum: Grapevine, Texas. https://doi.org/10.2514/6.2017-1558*

*3.Boon MA, Drijfhout AP, Tesfamichael S (2017) Comparison of a fixed-wing and multi-rotor UAV for environmental mapping applications: A case study. Int. Arch. Photogramm Remote Sens Spatial Inf Sci 42:47-54. https://doi.org/10.5194/isprs-archives-XLII-2-W6-47-2017*

*4.Çakici F, Leblebicioğlu MK (2016) Control System Design of a Vertical Take-off and Landing Fixed-Wing UAV. IFACPapersOnLine 49(3):267-272. https://doi.org/10.1016/j.ifacol.2016.07.045*

*5.Cwojdziński L, Adamski M (2014) Power units and power supply systems in UAV. Aviation 18(1):1-18. https://doi.org/10.3846/16487788.2014.865938*

*6.Dwivedi YD, Waykar TMS, Varun L (2020) Aerodynamic Characterization Of Albatross-Inspired Airfoils/Wings. Int J Adv Sci Technol 29(12s):801-815.*

*7.Ebeid E, Skriver M, Jin J (2017) A Survey on Open-Source Flight Control Platforms of Unmanned Aerial Vehicle. Paper presented 2017 Euromicro Conference on Digital System Design (DSD). IEEE: Vienna, Austria. https://doi.org/10.1109/DSD.2017.30*

*8.Garcia-Nieto S, Velasco-Carrau J, Paredes-Valles F, Salcedo JV, Simarro R (2019) Motion equations and attitude control in the vertical flight of a VTOL bi-rotor UAV. Electronics 8(2):208. https://doi.org/10.3390/electronics8020208*

*9.Ge J, Liu L, Dong X, He Y (2021) A trajectory optimization method for reducing magnetic disturbance of an internal combustion engine powered unmanned aerial vehicle. Aerosp Sci Technol 116:106885. https://doi.org/10.1016/j.ast.2021.106885*

*10.Girishkumar G, McCloskey B, Luntz AC, Swanson S, Wilcke W (2010) Lithium-Air Battery: Promise and Challenges. J Phys Chem Lett 1(14):2193-2203. https://doi.org/10.1021/jz1005384*

*11.Goetzendorf-Grabowski T, Tarnowski A, Figat M, Mieloszyk J, Hernik B (2021) Lightweight unmanned aerial vehicle for emergency medical service – Synthesis of the layout. Proc Inst Mech Eng G J Aerosp Eng 235(1):5-21. https://doi.org/10.1177/0954410020910584*

*12.Gur O, Rosen A (2009) Optimizing Electric Propulsion Systems for Unmanned Aerial Vehicles. J Aircr 46(4):1340-1353. https://doi.org/10.2514/1.41027*

*13.Jing L, Tang W, Wang T, Ben T, Qu R (2022) Performance Analysis of Magnetically Geared Permanent Magnet Brushless Motor for Hybrid Electric Vehicles. Trans Transp Electrification 8(2):2874-2883. https://doi.org/10.1109/TTE.2022.3151681*

*14.Körpe DS, Kanat ÖÖ, Oktay T (2019) The Effects of Initial y plus: Numerical Analysis of 3D NACA 4412 Wing Using γ-Re θSST Turbulence Model. EJOSAT 17:692-702. https://doi.org/10.31590/ejosat.631135*

*15.Kubo D, Suzuki S (2008) Tail-Sitter Vertical Takeoff and Landing Unmanned Aerial Vehicle: Transitional Flight Analysis. J Aircr 45(1):292-297. https://doi.org/10.2514/1.30122*

*16.Kumar P, Sonkar S, Ghosh AK, Philip D (2020) Real-time vision-based tracking of a moving terrain target from Light Weight Fixed Wing UAV using gimbal control. Paper presented 2020 7th International Conference on Control, Decision and Information Technologies (CoDIT). IEEE: Prague, Czech Republic. https://doi.org/10.1109/CoDIT49905.2020.9263896*

*17.Li Y, Yang J, Song J (2017) Design principles and energy system scale analysis technologies of new lithium-ion and aluminum-ion batteries for sustainable energy electric vehicles. Renew Sust Energ Rev 71:645-651. https://doi.org/10.1016/j.rser.2016.12.094*

*18.Luongo CA, Masson PJ, Nam T, Mavris D, Kim HD, Brown GV, Waters M, Hall D (2009) Next generation more-electric aircraft: A potential application for HTS superconductors. IEEE Trans Appl Supercond 19(3):1055-1068. https://doi.org/10.1109/TASC.2009.2019021*

*19.Lyu X, Gu H, Wang Y, Li Z, Shen S, Zhang F (2017) Design and implementation of a quadrotor tail-sitter VTOL UAV. Paper presented 2017 IEEE International Conference on Robotics and Automation (ICRA). IEEE: Singapore. https://doi.org/10.1109/ICRA.2017.7989452*

*20.Matsumoto T, Kita K, Suzuki R, Oosedo A, Go K, Hoshino Y, Konno A, Uchiyama M (2010) A hovering control strategy for a tail-sitter VTOL UAV that increases stability against large disturbance. Paper presented 2010 IEEE International Conference on Robotics and Automation. Anchorage, United States. https://doi.org/10.1109/ROBOT.2010.5509183*

*21.McCormick BW (1999) Aerodynamics of V/STOL flight. North Chelmsford: Courier Corporation.*

*Nelson RC (1989) Flight Stability and Automatic Control. New York: WCB/McGraw Hill.Oh S, Park C, Nguyen D, Kim S, Kim Y, Choi Y, Lee J (2021) Investigation on the operable range and idle condition of hydrogen-fueled spark ignition engine for unmanned aerial vehicle (UAV). Energy 237:121645. https://doi.org/10.1016/jenergy.2021.121645*

*23.Oktay T, Eraslan Y (2021) Numerical Investigation of Effects of Airspeed and Rotational Speed on Quadrotor UAV Propeller Thrust Coefficient. J Aviat 5(1):9-15. https://doi.org/10.30518/jav.872627*

*Prouty RW (1995) Helicopter performance, stability, and control. Malabar: Krieger Publishing.*

*24.Prouty RW (1995) Helicopter performance, stability, and control. Malabar: Krieger Publishing.Rapinett A (2009) Zephyr: A High Altitude Long Endurance Unmanned Air Vehicle. (doctoral dissertation). Surrey: University of Surrey. In English.*

*25.Raymer DP (2018) Aircraft Design: A Conceptual Approach, Sixth Edition.*

*26.Reston: AIAA. https://doi.org/10.2514/4.104909*

*26..Robotics and Automation. Anchorage, United States. https://doi.org/10.1109/ROBOT.2010.5509183Roskam J (1985a) Airplane design. Lawrence: DARcorporation.*

*27.Roskam J (1985b) Airplane Design Part VII: Determination of Stability, Control and Performance Characteristics. Lawrence: DARcorporation.Saeed AS, Younes AB, Cai C, Cai G (2018) A survey of hybrid Unmanned Aerial Vehicles. Prog Aerosp Sci 98:91-105. https://doi.org/10.1016/j.paerosci.2018.03.007*

*28.Sonkar S, Kumar P, Philip D, Ghosh AK (2020) Low-Cost Smart Surveillance and Reconnaissance Using VTOL Fixed Wing UAV. Paper presented 2020 IEEE Aerospace Conference. IEEE: Big Sky, United States. https://doi.org/10.1109/AERO47225.2020.9172554*

*29.Sonkar S, Kumar P, Philip D, Ghosh AK (2021) Real-Time Video Processing System for Fixed-Wing UAV. Paper presented Proceedings of the International Conference on Optics and Electro-Optics. Springer: Dehradun, India. https://doi.org/10.1007/978-981-15-9259-1_67*

*30.Sonkar SK, Kumar P, George RC, Philip D, Ghosh AK (2022) Detection and Estimation of Natural Gas Leakage Using UAV by Machine Learning Algorithms. IEEE Sens J 22(8):8041-8049. https://doi.org/10.1109/JSEN.2022.3157872*

*31.Stone RH, Anderson P, Hutchison C, Tsai A, Gibbens P, Wong KC (2008) Flight Testing of the T-Wing Tail-Sitter Unmanned Air Vehicle. J Aircr 45(2):673-685. https://doi.org/10.2514/1.32750*

*32.Sun J, Li B, Jiang Y, Wen C-Y (2016) A Camera-Based Target Detection and Positioning UAV System for Search and Rescue(SAR) Purposes. Sensors 16(11):1778. https://doi.org/10.3390/s16111778*

*33.Wan AN, Sim GMS, Koh RWL, Koh RKF, Teo GT, Yap TH, Nilju T, Srigrarom S, Holzapfel F, Marvakov V, Bhadwaj P, Tantrairatn S, Sakulthong S (2019) Development of UGS-TUM Vertical Take off Landing (VTOL) Drone with Flight Control. Paper presented 2019 1st International Symposium on Instrumentation, Control, Artificial Intelligence, and Robotics, ICA SYMP. IEEE: Bangkok, Thailand. https://doi.org/10.1109/ICA-SYMP.2019.8646176*

*34.Xie Y, He S, Savvaris A, Tsourdos A, Zhang D, Xie A (2022) Convexification in energy optimization of a hybrid electric propulsion system for aerial vehicles. Aerosp Sci Technol 123:107509. https://doi.org/10.1016/j.ast.2022.107509*

*35.Zhang H, Wang L, Tian T, Yin J (2021) A Review of Unmanned Aerial Vehicle Low-Altitude Remote* Sensing (UAV-LARS)

*Sensing (UAV-LARS) Use in Agricultural Monitoring in China. Remote Sens 13(6):1221. https://doi.org/10.3390/rs13061221*

*36.Zong J, Zhu B, Hou Z, Yang X, Zhai J (2021) Evaluation and Comparison of Hybrid Wing VTOL UAV with Four Different Electric Propulsion Systems. Aerospace 8(9):256. https://doi.org/10.3390/aerospace809025*

# Experimental Investigation of the CFHT-27 Cusped-Field Hall Thruster Performance

**Emin Saridede1 , Selcen Yediyildiz1 , Murat Celik1,***
1.Bogazici Universitesi – Department of Mechanical Engineering – Istanbul, Turkey

## A B S T R A C T

*Cusped-field Hall thrusters (CFHT) have significant potential for use in many space missions due to their simplicity, long life and high efficiency. CFHT-27, designed and developed at the Bogazici University Space Technologies Laboratory (BUSTLab), a prototype CFHT with a 27-mm diameter discharge channel. CFHT-27 utilizes samarium-cobalt (SmCo) permanent magnets. The thrust and efficiency of a cusped-field thruster is closely related to its size and design parameters. In this study, in order to understand the relationships between the design parameters and the thruster performance, the performance tests of the CFHT27 are carried out for a given magnetic field topology. The thruster was operated at discharge voltages ranging from 250 to 500V with argon propellant with up to 3,000 s of specific impulse. The measurements show that CFHT-27 can achieve thrust values from 1 to 46 mN. Thus, this thruster can be used for a wide range of thrust values allowing throttle capabilities for different missions.*

***Keywords: Electric propulsion; Plasma thrusters; Thrust stand; Performance measurements.***

## I. INTRODUCTION

In recent years electric propulsion systems are increasingly being employed for the propulsive needs of satellites and spacecraft due to their much higher specific impulse levels when compared with chemical thrusters (Lev et al. 2019; Martinez-Sanchez and Pollard 1998, Mazouffre 2016). Among various electric propulsion concepts, Hall-effect thrusters are the most used electric thrusters (Lev et al. 2019). Hall-effect thrusters use electric and magnetic fields for both the ionization of the neutral propellant gas, hence creating a plasma, and the acceleration of the charged atoms of this plasma to produce thrust. In Hall thrusters, the imposed magnetic field affects both the electrons and the ions. However, due to their much larger masses, the ions move mostly unaffected by the field and are accelerated away from the thruster by the applied axial electric field, whereas the electrons follow an azimuthal that is perpendicular to both the applied axial electric field and the radial magnetic field (Martinez-Sanchez and Pollard A cusped-field Hall thruster (CFHT) is a modified Hall thruster which was first studied by THALES Electron Devices in Germany (Koch et al. 2007; Kornfeld et al. 2003; 2007). This concept is also patented by Airbus Defence and Space GmbH (Hey et al. 2019). Based on the original design of THALES, researchers in academia have also investigated this thruster concept; at MIT (Courtney 2008; Courtney and Martinez-Sanchez 2007; Gildea et al. 2013; Matlock et al. 2010), at Stanford University

(MacDonald et al.2012), and at Harbin Institute of Technology (Liu et al. 2014a; b; Ma et al. 2015; Zhao et al. 2013). In this type of Hall unlike a single region of radial magnetic field of a typical Hall thruster, multiple regions of radial magnetic field are created by adopting alternating polarity permanent magnets. These radial magnetic field regions confine electrons that would normally move upstream to the anode. The electrons confined in the high radial magnetic field regions cause electron impact ionization of the neutral gas that is introduced to the discharge channel at the anode region. For these thrusters, due to the presence of multiple cusped regions, the discharge voltage can be much higher than that of a typical Hall thruster which only has a single cusped region (Courtney 2008; Kornfeld et al. 2006). Hence, in CFHTs, a wider range of thrust values can be obtained (Kornfeld et al. 2005). Furthermore, other researchers claimed that the cusped magnetic field in these thrusters can be effective in reducing the plasma wall interaction resulting in an increase in the thruster life (Gildea and Matlock 2013; Harmann et al. 2007).

Different studies have been conducted in order to understand the performance characteristics of CFHTs (Fahey et al. 2017; Hu et al.2016; Liang et al. 2019). These characteristics have been investigated depending on the magnetic field strength in the discharge channel (Hu et al. 2016) or on key design parameters that are set to obtain maximum efficiency, thrust and Isp. Four different configurations are analyzed for the permanent magnet rings with varying outer diameters. Results show that increasing magnetic field strength has a limiting effect on the radial cross-field electron current and it decreases the radial-width of the ionization region. Hence, the increase in the magnetic field strength reduces the propellant utilization as well as the performance of the thruster. It is also shown that the thrust and anode efficiency are positively affected in the case of weaker magnetic field strength in the discharge channel (Hu et al. 2016). Furthermore, an optimization with five different performance parameters are considered which include anode voltage, anode current, mass flow rate, magnet inner diameter and magnet outer diameter. For the anode current, an optimal value can be determined with the contribution of maximum anode potential and maximum mass flow rate. The results illustrate that the anode current and outer magnet radius have a significant effect on the performance. Regarding the location of the ionization regions, the differences in the discharge characteristics between cylindrical Hall thrusters and cusped-field thrusters using PIC-MCC simulations are investigated (Liang et al. 2019). The investigation indicates that the ionization regions of cusped-field thrusters move to the near-axis region and it has additional ionization in the plume region. In addition to these studies, also experimental measurements have been conducted on a divergent cusped-field thruster with a Faraday cup and a retarding potential analyzer to measure the ion current density and the ion energy distributions of the plume of the thruster (Gildea et al. 2013). The analyses show that the higher current density areas have more energetic and uniform ion groups. Nevertheless, it is also shown that these energetic ions are also thrown out at larger angles and cause an increase in the plume divergence. In the further stages of the

of the plume measurements, different cathode operating conditions are set and it is found that the cathode and the thruster operating conditions are closely linked. Also, time dependent anode current measurements indicate a significant difference for the high and low-current operation modes of the thruster. It is seen that in the case of lower current operation modes, the anode current seems to be less oscillatory.

For the cylindrical Hall thruster, the ionization and acceleration regions are both near the anode and are coupled to each other (Raitses et al. 2010). However, for the cusped field thruster, the acceleration region and the ionization region are separated from each other. The cusped field thruster also has wider throttling ability due to lower anode electron energy deposition (Cui et al. 2018).

Previous research show that magnetic topology plays an important role in the performance and efficiency of CFHTs (Ma et al.

2015; Hu et al. 2016; Liang et al. 2019; Ma et al. 2013). In CFHTs, electrons emitted from the cathode reach the discharge channel and motion of the electrons are impeded by the cusped magnetic field regions. From the literature, a typical CFHT contains three radial magnetic field regions, which could be considered as the ionization regions. The first one is located at the exit plane of the thruster ionization chamber and the other two of these regions are located inside the ionization chamber. The optimal location of the two inner ionization regions is not very well understood. Hence in the literature the length between these ionization regions vary for different cusped-field thrusters (Koch et al. 2007; Courtney and Martinez-Sanchez 2007; MacDonald et al. 2012, Hu et al.

2016; Liang et al. 2019). Even though there are three separate cusped regions, the region at the exit of the cylindrical discharge chamber affects the divergence of the plume and a relatively lower number of electrons are trapped in this region. Because of that, the effective cusped regions are the ones inside the chamber. The topology of the exit magnetic cusp can be modified to control the plume divergence and can be used to increase thrust efficiency (Liu et al. 2014b).

For a CFHT, the paths of electrons are illustrated in Fig. 1, which shows the electrons leaving the cathode move upstream towards the positively biased anode. The presence of the cusp shaped radial magnetic field created by the permanent magnets impedes the motion of these backstreaming electrons creating an azimuthal electron current due to Hall effect in the regions of perpendicular electric and magnetic fields

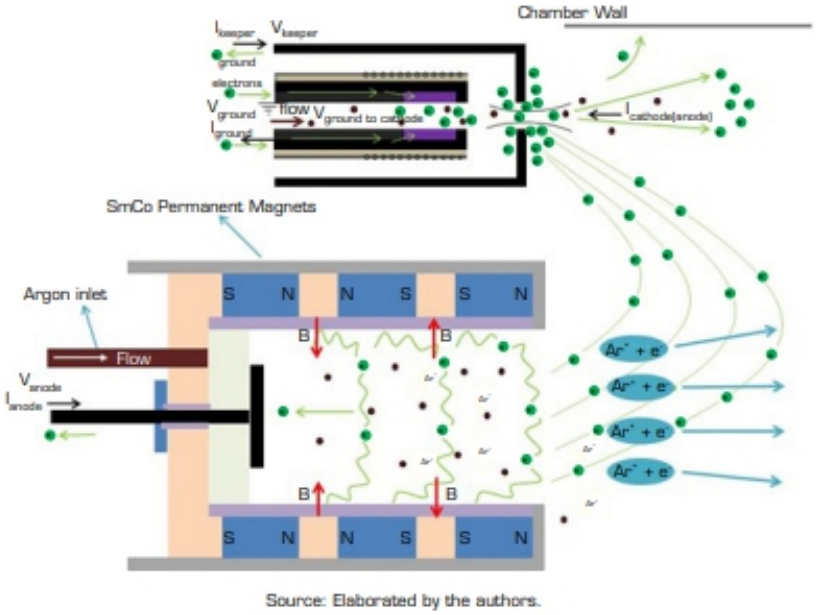


Source: Elaborated by the authors.

**Figure 1.** Schematic of the electron flow in a typical CFHT with double cusped region.

Based on the research presented in the literature, a prototype CFHT with a cylindrical discharge chamber diameter of 27 mm was designed and manufactured. The magnetic topology and the strength of the magnetic field is determined after a thorough review of the scientific literature in this field. Performance measurements of this thruster, called CFHT-27, are conducted inside the Bogazici University Space Technologies Laboratory (BUSTLab) vacuum chamber using an in-house built thrust stand. The operational parameters of the thruster were investigated for varying discharge voltage and propellant flow rate values. In this study, the range of thrust values that can be obtained with this thruster and its throttling ability, for determining its suitability for space mission, are investigated.

## CFHT-27 CUSPED-FIELD HALL EFFECT THRUSTER

CFHT-27 has quartz discharge chamber walls. The 1.5-mm thick chamber walls has an inner diameter of 27 mm and an outer diameter of 30 mm. The thruster employs 6 mm thick axially polarized samarium-cobalt (SmCo) permanent ring magnets with an inner diameter of 30 mm and an outer diameter of 40 mm. Between the ring magnets 1018 steel spacers are used because of their high permeability at low cost compared to alternatives such as pure iron or Hiperco-50A. Similarly, for the base plate 1018 steel is used. An aluminum casing is used to protect the magnetic circuit and to hold the parts in place. A schematic of CFHT-27 is shown in Fig. 2.

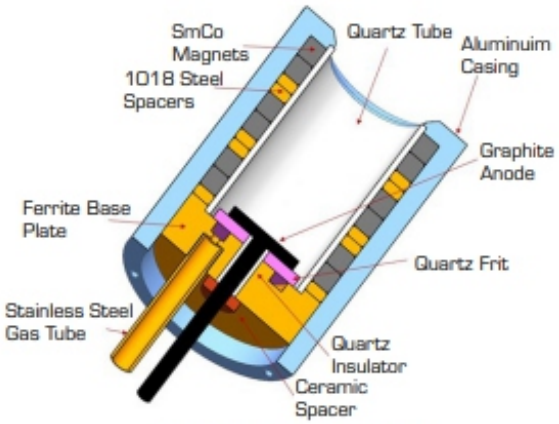


Source: Elaborated by the authors.

**Figure 2.** Schematic of CHFT-27 Hall effect thruster with materials used for each component.

The anode is made of graphite and is placed at the back wall. The diameter of the anode disc is 20 mm. The neutral gas enters the discharge channel through a 25-mm diameter porous quartz frit with a porosity of 100 microns. In most other similar cusped field thrusters, the propellant gas flows to the discharge chamber through the holes in the anode which is made of a conducting material (Ma et al. 2013; 2015; Peng et al. 2020). In the presented design, the porous nature of the quartz frit allows uniform distribution of neutral gas as it enters the discharge channel.

The CFHT-27 was operated using a LaB6 hollow cathode that is developed at BUSTLab (Kokal et al. 2021; Kurt et al. 2017). The cathode employs a 2-mm inner diameter, 4-mm outer diameter, LaB6 tube of 10 mm length placed inside a graphite cathode tube of 6 mm outer diameter 48 mm of length. The cathode is heated using a tantalum wire heater of a special design (Kurt et al.2017). For the operation of the thruster, the exit orifice of the hollow cathode is located 22 mm axially and 38 mm radially away from the center point of the thruster exit plane. For the tests discussed in this paper, the cathode mass flow rate is set to 4 standard cubic centimeters per minute (sccm) and cathode keeper current is kept at 1.5 A.

For simulating the magnetic field topology, COMSOL Multiphysics AC/DC module was used. Since the magnets are permanent SmCo magnets, the physics is chosen to be magnetic fields, no currents and meshing is done with physics-controlled finer mesh. Considering the permanent magnets, magnetic flux conservation for each magnet is defined separately and the remanent flux densities are identified from the material properties of SmCo and this value is given as 1.05 Tesla. Figure 3 shows the magnetic field topology of CFHT-27. Effect of the magnets closest to the discharge chamber exit plane on the magnetic field lines in the plume region magnetic topology are observed closely, since the magnetic field lines in this region direct the electrons flowing from the cathode to the discharge channel

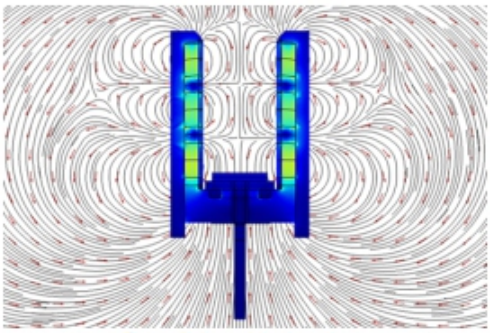

Source: Elaborated by the authors.

**Figure 3.** Magnetic field topology of CFHT-27.

The 2-2-2 magnetic field configuration is investigated for the SmCo permanent magnets and ferrite spacers. The magnetic topology results are presented in this study. In this configuration, the green parts are the SmCo magnets and the blue spaces in between are the ferrite spacers. One can observe that there are two separatrix lines between the cusped regions. These cusped regions are for the sufficient ionization of the gas. The cathode is placed along the diverging plume at the magnetic field lines along the exit of the thruster but not close to the main separatrix region, which is directly in the middle of the thruster. Nearly no divergence is observed for the 2-2-2 configuration in the middle part of the thruster. However, the magnet configurations can be changed to decrease the plume divergence at the outer exit in further study, since this leads to a decrease in the thrust because of the thrust vector. The magnetic field strength in a given stage increases as the total length of that magnet stage is increased. In the configuration presented in Fig. 3, the magnetic field strength at the cusp regions goes up to 1400 Gauss. A more detailed report about the effect of alternative magnetic field topology configurations and the strength at the exit to decrease the plume divergence will be presented as a separate study in the future.

## EXPERIMENTAL MEASUREMENTS AND DISCUSSION

The tests of the CFHT-27 are conducted inside the BUSTLab vacuum chamber, which is 1.5 m in diameter and 2.7 m in length (Korkmaz et al. 2015). The picture of the BUSTLab vacuum chamber used for the tests of the CFHT-27 is shown in Fig. 4. During the tests, the pressure inside the vacuum chamber was $6.2 \times 10{-}5$ torr when operating the thruster at 17 sccm anode flow and 4 sccm cathode flow of argon propellant. Picture from the tests of the thruster is shown in Fig. 5. The plume divergence angle decreases, when the separatrix gets a slope perpendicular to the direction of the electric field created due the anode voltage (Ma et al. 2015; Zhurin et al. 1999). Based on the discussion from the literature, the main plasma regions are between the bright edges of the plume regions (Ma et al. 2015). Thus, the region between the bright edges of the plume can be considered as the main ion beam region. From the visual inspection of the plume, the divergence angle is estimated to be about 32°.

Source: Elaborated by the authors.

**Figure 4.** BUSTLab vacuum chamber.

Source: Elaborated by the authors.

**Figure 5.** Picture of CFHT-27 in operation inside the vacuum chamber.

Thrust MeasurementsAs mentioned before, thrust measurements of the CFHT-27 were conducted using in-house built inverted pendulum type thrust stand (Kokal and Celik 2017a; b). The resolution for the thrust measurements was ± 0.296 mN. The thrust stand system uses a Linear Variable Differential Transformer (LVDT) sensor to measure the displacement of the inverted pendulum structure due to the force produced by the thruster. This displacement information with the premeasured stiffness value of the system gives the created thrust value. The thrust is measured in such a way that the LVDT displacement value is recorded when the anode voltage, hence the electric field, is applied. Thus, thrust due to the momentum of the Argon gas before the application of the voltage to the anode is accounted separately. Since the BUSTLab vacuum chamber employs cryogenic pumps for keeping the chamber background pressure at reasonably low levels during the thruster's operation, perturbations caused by the operation of the cryopumps cause noise during LVDT signal data reading. Because of that for certain thrust measurements, the cryopumps were turned off for short periods of time without affecting the pumping capacity and hence the chamber background pressure.

The measured thrust levels versus the applied anode voltage for various flow rates are shown in Fig. 6. As expected, with increasing anode voltage the generated thrust increases. This is expected, as the ions are accelerated to higher exit velocities. In addition to the increased ion exit velocities, increase of anode voltage would also increase the rate of ionization inside the ionization chamber of the thruster due to increase in the frequency of ionization collisions with the increase of both in the temperature of electrons as well as the energy of the created ions. Similarly, increase in the propellant flow rate to the anode results in increased thrust. As the flow rate is increased, the slope of the thrust versus anode voltage line shows slight increase. Figure 7 shows the measured thrust levels versus the propellant flow rate to the anode for various anode voltages. As seen in this figure, the slope of the thrust versus anode flow rate curve becomes steeper as the applied anode voltage is increased. Hence, at higher applied anode voltages, the range of thrust values that can be obtained becomes wider, as seen in Fig. 7.

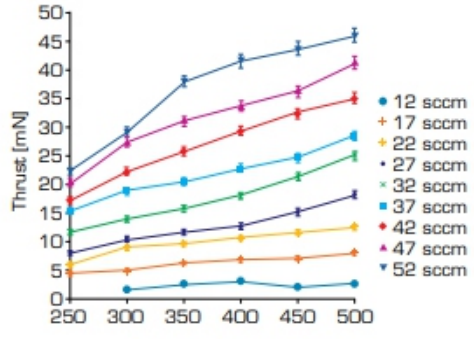


Source: Elaborated by the authors.

**Figure 6.** CFHT-27 thrust versus anode voltage.

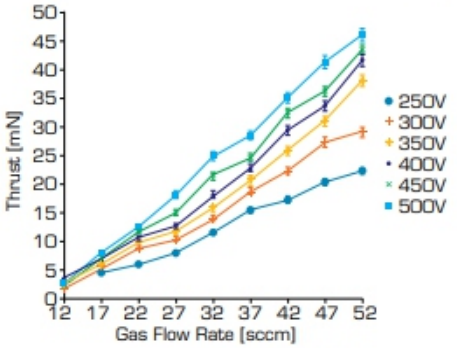


Source: Elaborated by the authors.

**Figure 7.** CFHT-27 thrust versus anode flow rate.

Based on the measured anode current and thrust values, the anode efficiency, $\eta_{anode}$, is calculated using:

$$\eta_{anode} = \frac{T^2}{2\dot{m}_a V_a I_a} \quad (1)$$

where T is the measured thrust, m.a is the set anode mass flow rate, Va is the set anode voltage and Ia is the measured anode current. Similarly, the specific impulse of anode only, Isp is calculated using:

$$I_{sp} = \frac{T}{\dot{m}_a g} \quad (2)$$

where g is the earth's specific gravity.

In Fig. 8, the general behavior of the anode current, anode power, specific impulse of anode only, Isp , and the anode efficiency, ηanode, versus applied anode voltage can be seen for varying anode propellant flow rate. Similarly, in Fig. 9 the same performance characteristics are presented versus the anode propellant flow rate for varying applied anode voltage. In Fig. 8a, it is seen that the anode current remains almost constant for varying anode voltages for a set anode flow rate value. As the anode flow rate increases, the anode current increases, as would be expected. On the other hand, Fig. 9a shows that the change in the anode voltage has a small effect on the anode current for a set of anode propellant flow rate value valves whereas the increase in the discharge current is almost linear with the change in the flow rate.

As seen in Figs. 8b and 9b, the power increases with increasing anode flow rate, and this increase is steeper for higher flow rates. As seen from these figures that this thruster has been operated at a very wide range of power values. The calculated Isp values, except for the 12 sccm flow rate are shown in Figs. 8c and 9c. As expected, the specific impulse increases for increased anode voltage. The observed Isp values vary between 500 to above 3,000 s, indicating a wide range of propellant utilization efficiency levels for varying discharge voltage and propellant flow rate values. With the selection of an appropriate Isp value, hence appropriate discharge voltage and propellant flow rate, a better performance can be expected from CFHT-27. This feature can be important when making decision on what type of a mission a specific thruster would be suitable for.As shown in Fig. 8d, CFHT-27 displays a general trend of increasing efficiency with increasing anode voltage. Thus, the figure shows that as the anode voltage is increased, the thruster performance increases. This is an expected result since as the discharge voltage is increased the ionization rate increases which improves the anode efficiency. Similarly, Figure 9d shows that as the anode flow rate increases the efficiency increases. The relationship between the thrust and the anode propellant flow rate is almost linear. Hence, it can be inferred from the figures that the flow rate where the leveling of the measured thrust was not reached in the scope of the experiments conducted as part of this study. The flow rates where the thrust value levels off must be at higher flow rates, hence it can be inferred that the thruster can handle higher flow rates and hence higher thrust values. Therefore, a wide working range thrust values than measured as part of this study can be expected from this thruster making it a suitable candidate for a wider range of space missions.Figures 8d and 9d show that the efficiency tends to increase with increasing anode flow rate. These two graphs can point that CFHT-27 can produce higher thrust values, and again this would widen the range of thrust values and hence its

It is a desired result for CFHT27, because even if it is a small thruster in size, it can be used in a wider range of space missions than would be expected for such a small thruster. It is observed that for higher discharge voltages the efficiency is also improved, hence a higher performance thruster is achieved.

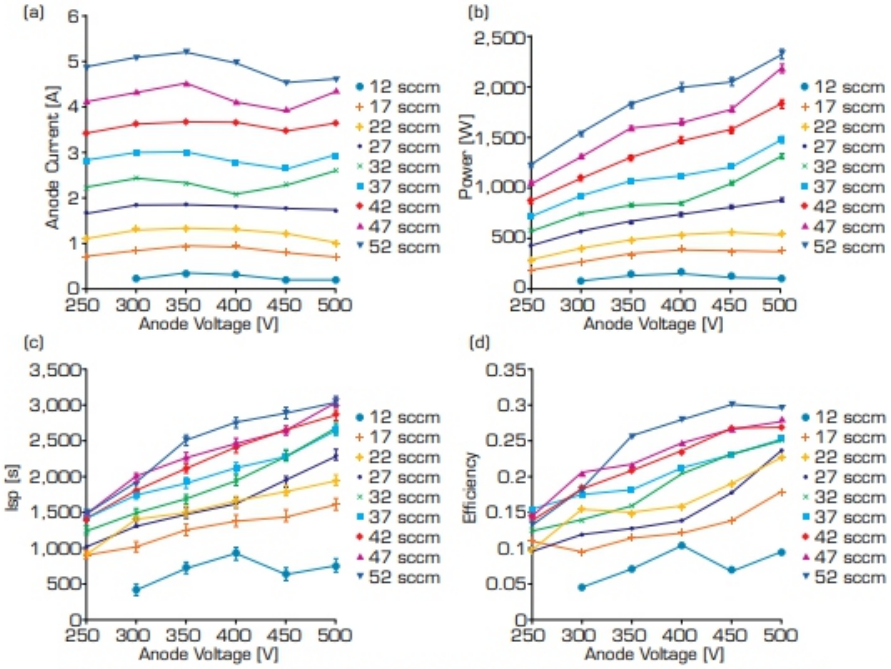


**Figure 8.** CFHT-27 performance measurement results for varying anode voltage rate values. (a) Anode current versus anode voltage, (b) Anode power versus anode voltage, (c) Anode specific impulse versus anode voltage, (d) Anode efficiency versus anode voltage.

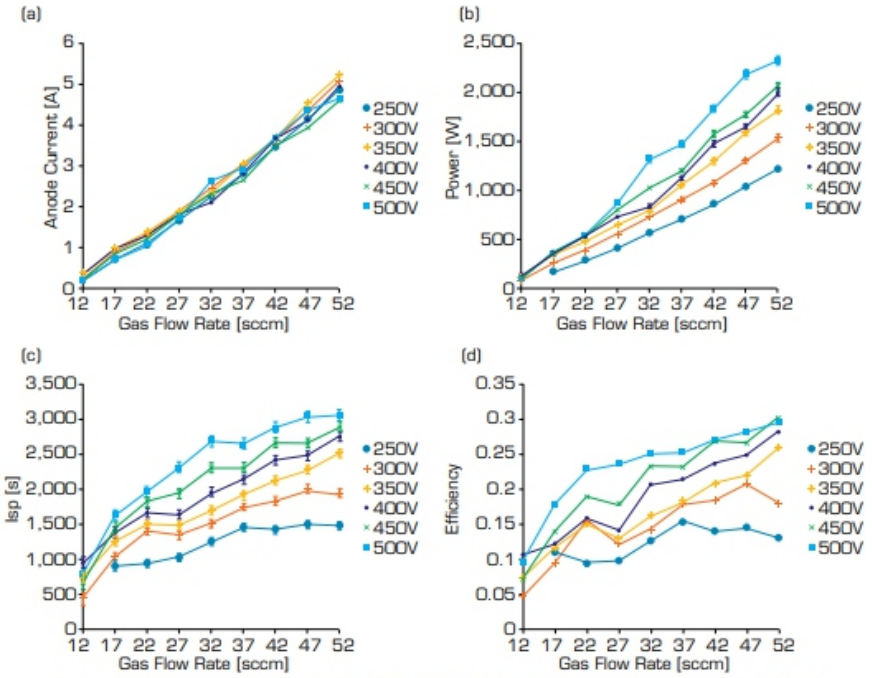


**Figure 9.** CFHT-27 performance measurement results for varying anode flow rate values. (a) Anode current versus anode flow rate, (b) Anode power versus anode flow rate, (c) Anode specific impulse versus anode flow rate, (d) Anode efficiency versus anode flow rate.

As seen in Fig. 8b and Fig. 7, as the flow rate increases the anode current and the thrust increase. For the configuration tested in this report, for 52 sccm anode flow rate at 500 V discharge voltage, the measured thrust is 46 mN corresponding to a specific impulse of 3,037 s at an anode power of 2,320 W with 29.6% anode efficiency. As observed, the increase in the anode flow rate increases the thrust; however, if the flow rate is further increased, after a certain flow rate it is expected that the rate of increase in thrust will drop.

In addition to changing the anode voltage and the anode flow rate for the investigation of the performance of this thruster, via altering the magnetic topology and the separatrix angle at the cusped region near the exit plane of the discharge chamber a better performance characteristic can be found. However, the focus of this study was limited to presenting a predetermined magnetic field topology and alteration to magnetic field topology is left as a separate study.

## CONCLUSION

This paper presents the performance measurements of the CFHT-27 for a predetermined magnetic field topology. The thruster was operated using Argon as the propellant. During the tests, the anode flow rate was varied from 12 to 52 sccm with 5 sccm increments and the discharge voltage was varied from 250 to 500 V with 50 V increments. The measured thrust values have a wide range from 1 to 46 mN indicating an almost continuous range of thrust values obtainable for this thruster. Such a wide range of thrust values at reasonable anode efficiency values make this thruster an attractive candidate for space missions where high throttleability is desired.

A more detailed report about the effect of alternative magnetic field topology configurations will be presented as a separate study in the future.

## CONFLIT OF INTEREST

Nothing to declare.

## AUTHORS' CONTRIBUTION

Conceptualization: Saridede E, Yediyildiz S and Celik M; Methodology: Saridede E and Celik M; Software Saridede E; Validation: Saridede E; Formal analysis: Saridede E and Yediyildiz S; Investigation: Saridede E, Yediyildiz S and Celik M; Resources: Saridede E and Celik M; Data Curation: Saridede E and Celik M; Writing – Original Draft: Saridede E, Yediyildiz S and Celik M; Writing – Review & Editing: Saridede E and Celik M; Visualization: Saridede E and Yediyildiz S; Supervision: Celik M; Project administration: Celik M; Funding acquisition: Celik M

## DATA AVAILABILITY STATEMENT

The data will be available upon request.

**FUNDING**

Scientific and Technological Research Council of Turkey

[https://doi.org/10.13039/501100004410]

Grant No: 214M572

**ACKNOWLEDGEMENTS**

Not applicable.

**REFERENCES**

*1.Courtney DG (2008) Development and characterization of a diverging cusped field thruster and a lanthanum hexaboride hollow cathode (master's thesis). Cambridge: Massachusetts Institute of Technology. [accessed May 5 2022]. http://hdl.handle.net/1721.1/45239*

*2.Courtney DG, Martinez-Sanchez M (2007) Diverging cusped-field Hall thruster (DCHT). Paper presented Proceedings 30th International Electric Propulsion Conference. Florence, Italy.*

*3.Cui K, Liu H, Jiang WJ, Sun QQ, Hu P, Yu DR (2018) Effects of cusped field thruster on the performance of drag-free control system. Acta Astronaut 144:193-200. https://doi.org/10.1016/j.actaastro.2017.12.032*

*4.Fahey T, Muffatti A, Ogawa H (2017) High fidelity multi-objective design optimization of a downscaled cusped field thruster. Aerospace 4(4):55. https://doi.org/10.3390/aerospace4040055*

*5.Gildea SR, Matlock TS, Martínez-Sánchez M, Hargus Jr WA (2013) Erosion measurements in a low-power cusped-field plasma thruster. J Propuls Power 29(4):906-918. https://doi.org/10.2514/1.B34607*

*6.Harmann HP, Koch N, Kornfeld G (2007) Low complexity and low cost electric propulsion system for telecom satellites based on HEMP thruster assembly. Paper presented Proceedings of the 30th International Electric Propulsion Conference. Florence, Italy.*

*7. Hey FG, Johann U, Kornfeld G (2019) Cusped-field thruster, US Patent 10,184,460.*

*8. Hu P, Liu H, Gao Y, Yu D (2016) Effects of magnetic field strength in the discharge channel on the performance of a multi cusped field thruster. AIP Advances 6(9):095003. https://doi.org/10.1063/1.4962548*

*9. Koch N, Harmann H, Kornfeld G (2007) Status of the THALES high efficiency multi stage plasma thruster development for HEMP-T 3050 and HEMP-T 30250. Paper presented Proceedings of the 30th International Electric Propulsion Conference. Florence, Italy.*

*10.Kokal U, Celik M (2017a) Development of a mili-Newton level thrust stand for thrust measurements of electric propulsion systems. Paper presented 2017 8th International Conference on Recent Advances in Space Technologies (RAST). IEEE; Istanbul, Turkey.*

*11.Kokal U, Celik M (2017b) Development of BUSTLab thrust stand for mili-Newton level thrust measurements of electric propulsion systems. Paper presented 35th International Electric Propulsion Conference. Atlanta, GA, USA.*

*12.Kokal U, Turan N, Celik M (2021) Thermal analysis and testing of different designs of LaB6 hollow cathodes to be used in electric propulsion applications. Aerospace 8(8):215. https://doi.org/10.3390/aerospace8080215*

*13.Korkmaz O, Jahanbakhsh S, Celik M, Kurt H (2015) Space propulsion research vacuum facility of the Bogazici University Space Technologies Laboratory. Paper presented 2015 7th International Conference on Recent Advances in Space Technologies (RAST). IEEE; Istanbul, Turkey. https://doi.org/10.1109/RAST.2015.7208420*

*14. Kornfeld G, Harmann HP, Koch N (2005) Status and limited life test results of the cylindrical HEMP 3050 thruster. Paper presented 41st AIAA/ASME/SAE/ASEE Joint Propulsion Conference & Exhibit. AIAA; Tucson, AZ, USA. https://doi.org/10.2514/6.2005-4223*

*15. Kornfeld G, Koch N, Coustou G (2003) First test results of the HEMP thruster concept. Paper presented Proceedings of the 28th International Electric Propulsion Conference, 2003.*

*16. Kornfeld G, Koch N, Harmann HP (2007) Physics and evolution of HEMP-thrusters. Paper presented Proceedings of the 30th International Electric Propulsion Conference, Florence, Italy.*

*17.Kornfeld G, Koch N, Harmann HP, Micheli P, Meusemann H, Gengembre E (2006) High power HEMP-thruster module, status and results of a DLR and ESA development program. Paper presented 42nd AIAA/ASME/SAE/ASEE Joint Propulsion Conference & Exhibit. AIAA; Sacramento, CA, USA. https://doi.org/10.2514/6.2006-4476*

*18. Kurt H, Kokal U, Turan N, Celik M (2017) Note: Coaxial-heater hollow cathode. Rev Sci Instrum 88(6):066103. https://doi.org/10.1063/1.4986111*

*19.Lev D, Myers RM, Lemmer KM, Kolbeck J, Koizumi H, Polzin K (2019) The technological and commercial expansion of electric propulsion. Acta Astronaut 159:213-227. https://doi.org/10.1016/j.actaastro.2019.03.058*

*20.Liang S, Liu H, Yu D (2019) Effect of magnetic field configuration on discharge characteristics in permanent magnet thrusters with cusped field. Paper presented 36th International Electric Propulsion Conference. Vienna, Austria.*

*21.Liu H, Sun G, Zhao Y, Chen P, Ma C, Wu H, Yu D (2014a) Plume control of a cusped field thruster. IEEE Trans Plasma Sci 43(1):127-129. https://doi.org/10.1109/TPS.2014.2360015*

*22.Liu H, Wu H, Zhao Y, Yu D, Ma C, Wang D, Wei H (2014b) Study of the electric field formation in a multi-cusped magnetic field. Phys Plasmas 21(9):090706. https://doi.org/10.1063/1.4896250*

*23. Ma C, Liu H, Hu Y, Yu D, Chen P, Sun G, Zhao Y (2015) Experimental study on a variable magnet length cusped field thruster. Vacuum 115:101-107. https://doi.org/10.1016/j.vacuum.2015.02.007*

*24. Ma C, Liu H, Yu D, Zhao Y, Chen P, Sun G (2013) Experiment research on a variable magnet length cusped field thruster. Paper presented 33rd International Electric Propulsion Conference. Washington, DC, USA.*

*25.MacDonald N, Young C, Cappelli M, Hargus Jr WA (2012) Ion velocity and plasma potential measurements of a cylindrical cusped field thruster. J Appl Phys 111(9):093303. https://doi.org/10.1063/1.4707953*

*26. Martinez-Sanchez M, Pollard JE (1998) Spacecraft electric propulsion – an overview. J Propuls Power 14(5):688-699. https://doi.org/10.2514/2.5331*

*27.Matlock T, Gildea SR, Hu F, Becker N, Lozano P, Martinez-Sanchez M (2010) Magnetic field effects on the plume of a diverging cusped-field thruster. Paper presented 46th AIAA/ASME/SAE/ASEE Joint Propulsion Conference & Exhibit. Nashville, TB, USA. https://doi.org/10.2514/6.2010-7104*

*28.Mazouffre S (2016) Electric propulsion for satellites and spacecraft: established technologies and novel approaches. Plasma Sources Sci Technol 25(3):033002. https://doi.org/10.1088/0963-0252/25/3/033002*

*29.Peng H, Daren Y, Yan S (2020) Magnet stage optimization of 5 kW multi-cusped field thruster. Plasma Sci Technol 22(9):094015. https://doi.org/10.1088/2058-6272/aba680Raitses Y, Merino E, Fisch NJ (2010) Cylindrical Hall thrusters with permanent magnets. J Appl Phys 108(9):093307. https://doi.org/10.1063/1.3499694*

*30.Zhao Y, Liu H, Yu D, Ma C (2013) Particle-in-cell simulations for a variable magnet length cusped-field thruster. Paper presented Proceedings 31st International Electric Propulsion Conference.*

*31.Zhurin VV, Kaufman HR, Robinson RS (1999) Physics of closed drift thrusters. Plasma Sources Sci. Technol 8(1):R1. https://doi.org/10.1088/0963-0252/8/1/02*

# Study of Head-Pursuit Cooperative Guidance Law for Near-space Hypersonic Interceptor

**Chenqi Zhu1,* Xiang Liu2**

1.Henan University of Science and Technology – School of Information Engineering – Luoyang – China.2.China State Shipbuilding Corporation – 2th laboratory 713th Research Institute – Zhengzhou – China.

## ABSTRACT

*In order to intercept hypersonic vehicles in near-space, a head-pursuit cooperative guidance law is proposed in this paper. Firstly, interceptors are regarded as multi-agents, and the communication relationship between them is represented by graph theory. Based on the time consistency theory of multi-agent system and sliding mode theory, a guidance law is designed along line-of-sight (LOS) to ensure the time cooperation of interceptors. Secondly, considering the requirement of the head-pursuit theory to the lead angle, a finite-time guidance law is designed perpendicular to LOS to ensure that each interceptor can complete head-pursuit interception. For the purpose of improving the intercept precision, extended state observers are used to estimate the system disturbances. The correctness of the guidance law is analyzed by Lyapunov stability theory. Finally, numerical simulations are presented and the results further verify the correctness of the guidance law.*

***Keywords: Multiagent system; Time consistency theory; Extended state observers; Finite-time guidance law.***

## I. INTRODUCTION

With the maturity of near-space technology, the advantage of hypersonic vehicle is becoming more and more obvious. Characteristics such as long flight distance, fast flight speed and strong maneuvering ability make the hypersonic vehicle have a strong ability of penetration. However, the traditional methods such as tail-chase interception and head-on interception have different deficiencies in the process of intercepting such targets. At the same time, with the development of antimissile system, it is difficult for a single interceptor to complete the combat tasks independently in the complex battlefield. In order to improve the interception probability for hypersonic vehicle, the cooperative interception of multiple interceptors is paid more attention to in the military field. As an important basic theory of multiagent cooperative guidance, the multiagent consistency theory achieved good results in the cooperative control of pilotless aircraft, autonomous vehicle, robot and other fields, which provides a theoretical basis for the study of head-pursuit cooperative guidance against hypersonic vehicles in near-space. Therefore, the research on head-pursuit cooperative guidance law based on multiagent consistency theory for near-space interceptor has great strategic value.

For the purpose of intercepting hypersonic vehicle effectively, a new interception method was proposed

by Golan and Shima (2004). This method required the interceptor to fly in the same direction as the target at a low speed in front of the target trajectory, so that the target can hit the interceptor from behind. Because the interceptor is in front of the target, this method is called head-pursuit interception. They used sliding mode control theory to design the guidance law and completed the headpursuit interception of the target. In order to attenuate the chattering phenomena caused by sliding mode control theory, Liu K et al. (2015) improved the head-pursuit guidance law based on double-power reaching law. For the purpose of improving the convergence rate of the guidance system, Si and Song (2017) proposed a head-pursuit guidance law based on fast double-power reaching law, which not only attenuated the system chattering, but also accelerated the convergence rate of the system. Since target maneuvering is unknown, Zhang et al. (2018) used an adaptive algorithm to estimate the system disturbance and presented a head pursuit guidance law based on time-scale separation which can improve system intercept accuracy and have strong robustness.

Taking into account the autopilot dynamics, Zhu and Guo (2019) proposed a head-pursuit guidance law based on back-stepping sliding mode, which further improved the interception accuracy. Based on this, Zhu (2021a) combined fractional order theory with sliding mode theory and proposed a head-pursuit guidance law based on fractional order sliding mode theory, which further weakened the chattering of the system. At the same time, Zhu (2021b) introduced the finite time disturbance observer into the design of head-pursuit guidance law, which ensured the system converge in finite time and improved the accuracy of the system.Cooperative guidance law for multiple missiles means that interceptors cooperate with each other in time and space complete the combat mission. Lee et al. (2007) proposed a guidance law that constrained both the attack time and angle with given values, which can intercept targets with low speed. Based on the optimal control theory, Sun and Xia (2012) proposed an optimal cooperative guidance law. L Feng et al. (2014) combined sliding mode theory with target strategy switching and proposed a cooperative guidance law based on two-layer design scheme, which carried out the cooperative control of attack time and angle. Cho et al. (2015) proposed an adaptive cooperative guidance law with a wide range of expected collision angles which can deal with the unknown target maneuver. Zhao et al. (2016) proposed a cooperative guidance law based on the finite-time consistency theory to ensure that multiple interceptors hit the target simultaneously. Based on this, Shi et al. (2018) introduced the second order sliding mode theory into the design of cooperative guidance law which weakened the chattering of the system effectively. Considering the communication between interceptors, Liu X and Liang (2019) designed a cooperative guidance law based on multiagent consistency principle to control the collision time and line-of-sight (LOS) angle. Up to now, most of the studies on cooperative guidance law focus on tail-chase interception and head-on interception, which is not suitable for the near-space interceptor, so that the interception rate against hypersonic vehicles in

near-space is not enough. Therefore, this paper studies this field and puts forward a head-pursuit cooperative guidance law for near-space interceptor.

## BACKGROUND INFORMATION AND PRELIMINARIES

Figure 1 is the relative motion schematic of head-pursuit interception in longitudinal plane, where points T and M are the target and the missile, r is the missile-target range, q is the LOS angle, θt and θm the lead angles, Vt and Vm velocities, the subscripts t and m denote the target and missile.

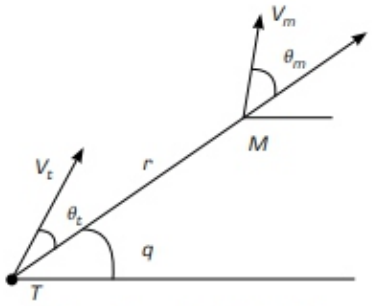


Source: Retrieved from Zhu (2021a).

**Figure 1.** Relative motion schematic.

Figure 2 is the relative motion schematic between multimissiles and target, where points T and Mi are the target and the missile i (i = 1, 2, ¼ n), where n is the number of missiles. ri is the distance between missile i and the target, qi is the LOS angle of missile I, θt and θmi are the lead angles of target and the missile I, Vt and Vmi are the velocities of target and the missile I.

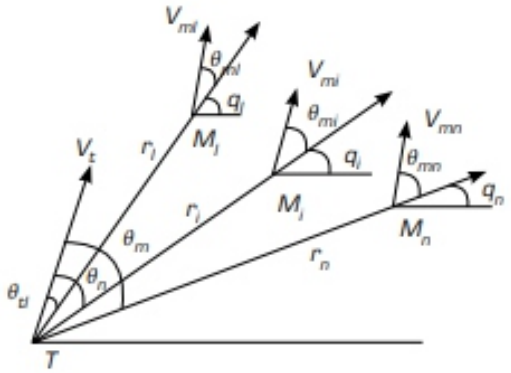


Source: Elaborated by the authors.

**Figure 2.** Relative motion schematic.

The control input can be projected along the LOS coordinate system. The projection along LOS is u1, and the projection perpendicular to LOS is u2. The control input can also be projected along the velocity coordinate system, am1 along velocity direction, and am2 perpendicular to velocity direction.According to Fig. 1, the relative equations of head-pursuit interception can be obtained in Eqs.

$$\dot{r} = V_m \cos\theta_m - V_t \cos\theta_t \tag{1}$$

$$\dot{q} = \left(V_m \sin\theta_m - V_t \sin\theta_t\right) / r \tag{2}$$

$$\dot{\theta}_t = \frac{a_t}{V_t} - \dot{q} \tag{3}$$

$$\dot{\theta}_m = \frac{a_{m2}}{V_m} - \dot{q} \tag{4}$$

where $a_t$ is the target acceleration.

Differentiating Eq. 1 with respect to time and combining with equation Eq. 2, Eq. 5 is given:

$$\ddot{r} - r\dot{q}^2 = (\dot{V}_m \cos\theta_m - a_{m2} \sin\theta_m) - (\dot{V}_t \cos\theta_t - a_t \sin\theta_t) \tag{5}$$

Let $u_1 = \dot{V}_m \cos\theta_m - a_{m2} \sin\theta_m$, and it is the projection of the control input along LOS.

The time-to-go of missile i is equal to the ratio of ri to .ri, where .ri represents the relative distance between missile i and the target, and .ri represents the change rate of the relative distance. Therefore, the time-to-go of missile i can be denoted by tgoi as Eq. 6

$$t_{goi} = -\frac{r_i}{\dot{r}_i} \qquad (i = 1,2,\cdots n) \tag{6}$$

where ri can be measured and .ri satisfies .ri = Vmi cosθmi – Vt sinθnBecause of the need for multimissiles to collide with the target at the same time, the predicted collision moment can be denoted by tfi as in Eq. 7.

$$t_{fi} = t - \frac{r_i}{\dot{r}_i} \qquad (i = 1,2,\cdots n) \tag{7}$$

Differentiating tfi with respect to time, Eq. 8 is given

$$\dot{t}_{fi} = \frac{r_i^2 \dot{q}_i^2}{\dot{r}_i^2} + \frac{r_i u_{1i}}{\dot{r}_i^2} + \frac{r_i(a_t \sin\theta_{it} - \dot{V}_t \cos\theta_{it})}{\dot{r}_i^2} \qquad (i = 1,2,\cdots n) \tag{8}$$

Let $d_i = (r_i (a_t \sin\theta_{it} - \dot{V}_t \cos\theta_{it}))/(\dot{r}_i^2)$ be the unknown system disturbance, then Eq. 8 can be written as in Eq. 9.

$$\dot{t}_{fi} = \frac{r_i^2 \dot{q}_i^2}{\dot{r}_i^2} + \frac{r_i u_{1i}}{\dot{r}_i^2} + d_i \qquad (i = 1,2,\cdots n) \tag{9}$$

Then, the relative motion equation of missile *I* to the target can be obtained as in Eqs. 10 and 11:

$$\begin{cases} \dot{r}_i = V_{mi} \cos\theta_{mi} - V_t \cos\theta_{it} \\ \dot{q}_i = (V_{mi} \sin\theta_{mi} - V_t \sin\theta_{it}) / r_i \\ \dot{\theta}_{it} = \dfrac{a_t}{V_t} - \dot{q}_i \\ \dot{\theta}_{mi} = \dfrac{a_{m2i}}{V_{mi}} - \dot{q}_i \end{cases} \tag{10}$$

$$\dot{t}_{fi} = \frac{r_i^2 \dot{q}_i^2}{\dot{r}_i^2} + \frac{r_i u_{1i}}{\dot{r}_i^2} + d_i \tag{11}$$

$$\lim_{t_i \to 0}(t_{fi} - t_{fj}) = 0; \quad (i = 1,2,\cdots n;\ j = 1,2,\cdots n) \tag{12}$$

According to the requirement of head-pursuit interception proposed by Golan and Shima (2004), each missile should satisfy the following formula (Eq. 13):

$$\lim_{t_i \to 0} \theta_{mi} = 0; \quad \lim_{t_i \to 0} \theta_{ti} = 0; \quad \theta_{mi} = \kappa \theta_{ti} \quad (i = 1,2,\cdots n) \tag{13}$$

where κ is a lead factor and satisfies κ > Vt/Vmi.In order to satisfy Eq. 12, the missiles can be seen as multiagents, the communication network of them can be represented by an undirected graph G = (ν, ζ, C), where ν represents a set of all nodes in G, z represents the lines that exist between all nodes in G, and ζ is the weight matrix of G. The entry of C is represented by Cij, if the information can be exchanged directly between agent i and agent j, the value of cij is 1, otherwise the value of cij is 0. In particular, cii = 0. If there is a line for information exchange between any agent, the undirected graph is defined as connected. Before giving the cooperative guidance law, some lemmas related to the finite-time consistency of multiagent are introduced.Lemma 1 (X Feng and Long 2007): For the following first-order multiagent system (Eq. 14):

$$\dot{x}_i = \upsilon_i \quad (i = 1,2,\cdots n) \tag{14}$$

where xi and uiare the state and control input of agent i respectively. When the undirected graph G is connected, and if the control input ui satisfies υi = sigδi [∑nj=1 cij (xj - xi)], where 0 < ζi < 1. Then there exists a finite time T*, such that when the time satisfies t > T*, the state of any agent j satisfies xj(t) = x*, where x* is a real number. The control input vi is called the finite-time consistency protocol for multiple agents.Lemma 2 (Yu et al. 2005): For the following nonlinear time-varying system (Eq. 15):

$$\dot{z}(t) = f(z,t), z \in \mathrm{R} \tag{15}$$

z is the system state and t is the time. Supposing that there is a continuous positive-definite function V(x), and this function satisfies the following differential inequality (Eq. 16)

$$\dot{V}(z) \le -\mu V(z) - \lambda V^{\alpha}(z) \tag{16}$$

where $\mu,\lambda > 0, 0 < \alpha < 1$ are constants, and $z(0) = z0$. The convergence time T of the system satisfies the following inequality (Eq. 17):

$$T \le \frac{1}{\mu(1-\alpha)} \ln \frac{V^{(1-\alpha)}(z_0)+\lambda}{\lambda} \tag{17}$$

Note 1: The target and missile are point masses, and the target velocity is a constant.

Note 2: The interceptor is in free flight if the distance satisfies $r \le 100$.

Note 3: If the distance satisfies $0.1 \le r \le 0.25$, it is considered that the missile has collided with the target.

Note 4: The function $sig\delta i(\bullet)$ is defined as $sig\delta i(\bullet) = |\bullet|\delta i\, sig(\bullet)$ .

## DESIGN OF HEAD-PURSUIT COOPERATIVE GUIDANCE LAW

In this part, a head-pursuit cooperative guidance law is proposed based on time consistency theory of multiagent system and sliding mode theory, and the stability is analyzed by Lyapunov stability theory.

### Design of guidance law along LOS

In this section, the guidance law along LOS is designed to ensure that the collision time of each missile tends to be consistent. At the same time, the disturbance is estimated by the extended state observer to improve the accuracy of the guidance law. Firstly, an extended state observer is designed as follows to estimate the disturbance di in Eq. 11 (Eq. 18)

$$\begin{cases} e_{ti} = z_{ti} - t_{fi}\,; \quad e_{di} = z_{di} - d_i \\ \dot{z}_{ti} = z_{di}\beta_{1i}e_{ti} + \dfrac{r_i^2\dot{q}_i^2}{\dot{r}_i^2} + \dfrac{r_i u_{1i}}{\dot{r}_i^2} \\ \dot{z}_{di} = -\beta_{2i}sig^{\gamma_{1i}}(e_{ti}) \end{cases} \tag{18}$$

where eti and edi are the estimation errors, zti and zdi the estimated values of tft and di, $\beta 1i, \beta 2i$ and $0 < \gamma 1i < 1$ the observer parameters to be determined. According to Z Zhu et al. (2013), the disturbance di in Eq. 11 can be well estimated by Eq. 18.According to the time consistency theory of multiagent system, the integral sliding mode surface is designed in Eq. 19:

$$s_{1i} = t_{fi}(t) - t_{fi}(0) + \int_0^t -\mathrm{sig}^{\alpha_i}\left[\sum_{j=1}^{n} c_{ij}(x_j - x_i)\right] d\tau \tag{19}$$

where $0 < \alpha_i < 1$.

Differentiating Eq. 19 with respect to time yields, Eq. 20 is given.

$$\dot{s}_{1i} = \dot{t}_{fi}(t) - \mathrm{sig}^{\alpha_i}\left[\sum_{j=1}^{n} c_{ij}(x_j - x_i)\right] \tag{20}$$

Substituting Eqs. 11 into Eq. 20 yields, Eq. 21 is given.

$$\dot{s}_{1i} = \frac{r_i u_{1i}}{\dot{r}_i^2} + \frac{r_i^2 \dot{q}_i^2}{\dot{r}_i^2} - \mathrm{sig}^{\alpha_i}\left[\sum_{j=1}^{n} c_{ij}(x_j - x_i)\right] + d_i \tag{21}$$

Define a fast power reaching law as Eq. 22:

$$\dot{s}_{1i} = -k_{1i} s_{1i} - k_{2i} sig^{\lambda_{1i}}(s_{1i}) \tag{22}$$

where k1l and k2l are positive constants, $0 < \alpha li < 1$.Therefore, according to Eqs. 21 and 22, the control input can be obtained as shown in Eq. 23

$$u_{1i} = \frac{\dot{r}_i^2 \left\{ -k_{1i} s_{1i} - k_{2i} sig^{\lambda_{1i}}(s_{1i}) + \mathrm{sig}^{\alpha_i}\left[\sum_{j=1}^{n} c_{ij}(x_j - x_i)\right] - z_{di} \right\}}{r_i} - \frac{r_i^2 \dot{q}_i^2}{r_i} \tag{23}$$

**Theorem 1**

Consider Eq. 11, the guidance law Eq. 23 along LOS direction will make the estimated collision time converge to a same constant with in a finite time. The proof is shown below:Consider a Lyapunov function in Eq. 24:

$$V_{1i} = \frac{1}{2} s_{1i}^2 \tag{24}$$

According to Eqs. 19 and 23, the derivative of Eq. 24 can be got by Eq. 25:

$$\begin{aligned} \dot{V}_{1i} &= s_{1i}\dot{s}_{1i} \\ &= s_{1i}\left\{ \frac{r_i^2 \dot{q}_i^2}{\dot{r}_i^2} + \frac{r_i u_{1i}}{\dot{r}_i^2} + d_i - \mathrm{sig}^{\alpha_i}\left[\sum_{j=1}^{n} c_{ij}(x_j - x_i)\right] \right\} \\ &= s_{1i}\left[ -k_{1i} s_{1i} - k_{2i} sig^{\lambda_{1i}}(s_{1i}) - z_{di} + d_i \right] \\ &= -k_{1i} s_{1i}^2 - k_{2i} sig^{\lambda_{1i}+1}(s_{1i}) \\ &= -2k_{1i} V_{1i} - 2^{\frac{\lambda_{1i}+1}{2}} k_{2i} V_{1i}^{\frac{\lambda_{1i}+1}{2}} \end{aligned} \tag{25}$$

According to Lemma 2, the sliding variable s1i and its derivative .s1i will converge to zero in finite-time T1i which satisfies Eq. 26:

$$T_{1i} \le \frac{1}{2k_{1i}\left(1-\frac{\lambda_{1i}+1}{2}\right)} \ln \frac{V^{\left(1-\frac{\lambda_{1i}+1}{2}\right)}\left(s_{1i0}\right)+2^{\frac{\lambda_{1i}+1}{2}}k_{2i}}{2^{\frac{\lambda_{1i}+1}{2}}k_{2i}} \tag{26}$$

Then, differentiating Eq. 19 with respect to time, Eq. 27 is given:

$$\dot{i}_{fi}(t) = \mathrm{sig}^{\alpha_i}\left[\sum_{j=1}^{n} c_{ij}(x_j - x_i)\right], \quad (t > T_{1i}) \tag{27}$$

According to Lemma 1, the estimated collision time of each missile will converge to a same constant in a finite time.

**Design of guidance law perpendicular to LOS**

In order to ensure that each missile can collide with the target in the way of head-pursuit interception, a guidance law perpendicular to LOS is designed in this part. According Eq. 13, a new variable xi is introduced n Eq. 28:

$$x_i = \theta_{mi} - \kappa\theta_{ti} \tag{28}$$

Then, the following system can be got as Eq. 29:

$$\dot{x}_i = \frac{a_{m2i}}{V_{mi}} + (\kappa - 1)\dot{q}_i - \kappa\frac{a_t}{V_t} \tag{29}$$

Let ωi = -κ at/Vt be the unknown disturbance of system, and estimate it with the following extended state observer (Eq. 30).

$$\begin{cases} e_{xi} = z_{xi} - x_i \; ; \quad e_{\omega i} = z_{\omega i} - \omega_i \\ \dot{z}_{xi} = z_{\omega i} - \beta_{3i} e_{xi} + \dfrac{a_{m2i}}{V_{mi}} + (\kappa - 1)\dot{q}_i \\ \dot{z}_{\omega i} = -\beta_{4i} sig^{\gamma_{2i}}(e_{xi}) \end{cases} \tag{30}$$

where exi and ewi are the estimation errors, zxi and zwi the estimated values of xi and ωi, β3i, β4i and 0 < γ2i < 1 the observer parameters to be determined.Define the sliding surface as follows (Eq. 31)

$$s_{2i} = x_i \tag{31}$$

Differentiating Eq. 19 with respect to time yields, Eq. 32 is given:

$$\dot{s}_{2i} = \dot{x}_i \tag{32}$$

Substituting Eq. 29 into Eq. 20 yields, Eq. 33 is given:

$$\dot{s}_{2i} = \frac{a_{m2i}}{V_{mi}} + (\kappa - 1)\dot{q}_i - \kappa \frac{a_i}{V_i} \tag{33}$$

Define a fast power reaching law in Eq. 34:

$$\dot{s}_{2i} = -k_{3i} s_{1i} - k_{4i} sig^{\lambda_{2i}}(s_{2i}) \tag{34}$$

where $k_{3i}$ and $k_{4i}$ are positive constants, $0 < \lambda_{2i} < 1$. According to Eqs. 33 and 34, Eq. 35 can be got:

$$a_{m2i} = V_{mi}\left[-k_{3i} s_{1i} - k_{4i} sig^{\lambda_{2i}}(s_{2i}) - (\kappa - 1)\dot{q}_i - z_{\omega i}\right] \tag{35}$$

According to the relation between LOS coordinate system and velocity coordinate system, there exists the following transformation relationship (Eq. 36):

$$\begin{bmatrix} a_{m1i} \\ a_{m2i} \end{bmatrix} = \begin{bmatrix} \cos\theta_{mi} & \sin\theta_{mi} \\ -\sin\theta_{mi} & \cos\theta_{mi} \end{bmatrix} \begin{bmatrix} u_{1i} \\ u_{2i} \end{bmatrix} \tag{36}$$

Therefore, Eq. 37 can be obtained based on Eqs. 23, 35 and 36:

$$u_{2i} = \frac{V_{mi}\left[-k_{3i} s_{1i} - k_{4i} sig^{\lambda_{2i}}(s_{2i}) - (\kappa - 1)\dot{q}_i - z_{\omega i}\right] + u_{1i}\sin\theta_{mi}}{\cos\theta_{mi}} \tag{37}$$

**Theorem 2**

Consider Eq. (10), the guidance law Eq. (37) perpendicular to LOS will make the lead angles satisfy Eq. (13), which ensures that each missile collide with the target in the way of head-pursuit interception in finite time. The proof is shown below:Consider a Lyapunov function in Eq. 38

$$V_{2i} = \frac{1}{2} s_{2i}^2 \tag{38}$$

According to Eqs. 23, 31, 35 and 37, the derivative of Eq. 38 can be got (Eq. 39)

$$\begin{aligned} \dot{V}_{2i} &= s_{2i}\dot{s}_{2i} \\ &= s_{2i}\left[\frac{a_{m2i}}{V_{mi}} + (\kappa - 1)\dot{q}_i + \omega_i\right] \\ &= s_{2i}\left[-k_{3i}s_{2i} - k_{4i}sig^{\lambda_{2i}}(s_{2i}) - z_{ai} + \omega_i\right] \\ &= -k_{3i}s_{2i}^2 - k_{4i}sig^{\lambda_{2i}+1}(s_{2i}) \\ &= -2k_{3i}V_{2i} - 2^{\frac{\lambda_{2i}+1}{2}} k_{4i} V_{2i}^{\frac{\lambda_{2i}+1}{2}} \end{aligned} \tag{39}$$

According to Lemma 2, the sliding variable s2i and its derivative .s2i will converge to zero in finite-time T2i, and T2i satisfies Eq. 40:

$$T_{2i} \le \frac{1}{2k_{3i}\left(1 - \frac{\lambda_{2i}+1}{2}\right)} \ln \frac{V^{\left(1-\frac{\lambda_{2i}+1}{2}\right)}(s_{2i0}) + 2^{\frac{\lambda_{2i}+1}{2}} k_{4i}}{2^{\frac{\lambda_{2i}+1}{2}} k_{4i}} \tag{40}$$

Then, according to Golan and Shima (2004), the lead angle θmi will be consistent with κθti and converge to zero. Therefore, the interceptor will collide with the target in the way of head-pursuit interception. Theorem 2 is proved.Note 5: Because u1i and a2mi are not orthogonal, if they are used as the control input of the system directly, there will be cancelation. Therefore, u1i and u2i as shown in Eqs. 23 and 37 are used as the control inputs of the system.Note 6: Depending on the head-pursuit cooperative guidance law, the interceptor velocity can no longer be assumed to be constant.

## SIMULATIONS

In this section, the correctness of the head-pursuit cooperative guidance law is verified by mathematical simulation. Suppose that there are three missiles to intercept a hypersonic vehicle in near-space, missile 1 and missile 2 can communicate directly, missile 2 and missile 3 can communicate directly also. However, missile 1 can communicate with missile 3 only missile 2 indirectly. Therefore, based on graph

theory, the weight matrix of communication network is shown in Eq. 41.

$$C = \begin{bmatrix} 0 & 1 & 0 \\ 1 & 0 & 1 \\ 0 & 1 & 0 \end{bmatrix} \tag{41}$$

When the origin of the inertial coordinate system is shifted to the target, the information of the target is Xt(0) = 0 ,Yt (0) = 0 , Vt = 1600 m/s, θt1 (0) = 10°, at = 50 sin(0.25πt) m/s2 , missile 1 is Xm1 (0) = 3000,Ym1 (0) = 4000 ,Vm1 (0) = 1200 m/s, θm1 (0) = 10°, missile 2 is Xm2(0) = 2000, Ym2 (0) = 6000, Vm2 (0) = 1200 m/s, θm2 (0) = -20°,missile 3 is X_m3 (0)=2500 ,Ym3 (0) = 3000, Vm3 (0) = 1200 m/s, θm3 (0) = 50°. The parameters of the head-pursuit cooperative guidance law are κ=2 , αi = 0.95, λ1i = 0.9, λ2i = 0.35, k1i= k3i = 10, k2i = k4i = 0.4, β1i = β3i = 50, β2i = β4i = 150, γ1i = γ2i = 0.35. Figures 3–10 are the simulation results.

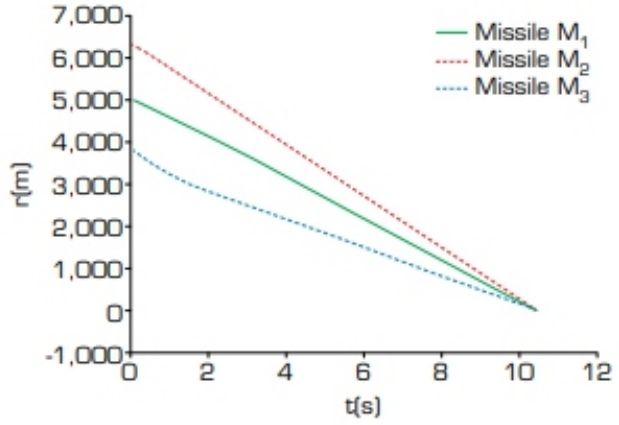


Source: Elaborated by the authors.

**Figure 3.** Range between missile and target

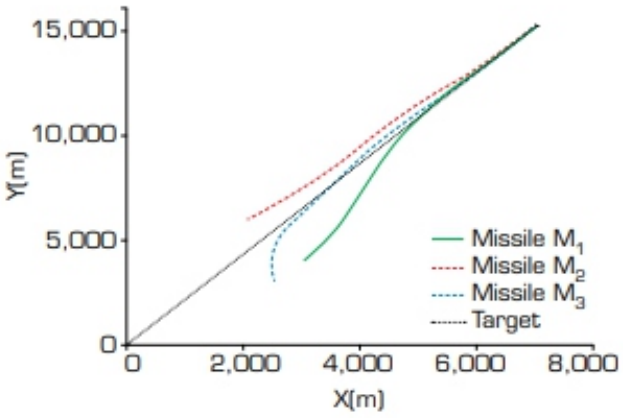


Source: Elaborated by the authors.

**Figure 4.** Relative motion orbit.

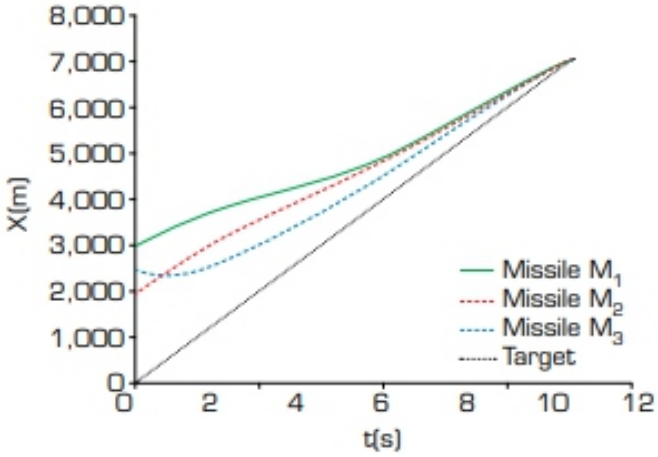


Source: Elaborated by the authors.

**Figure 5.** Change in the X-coordinate.

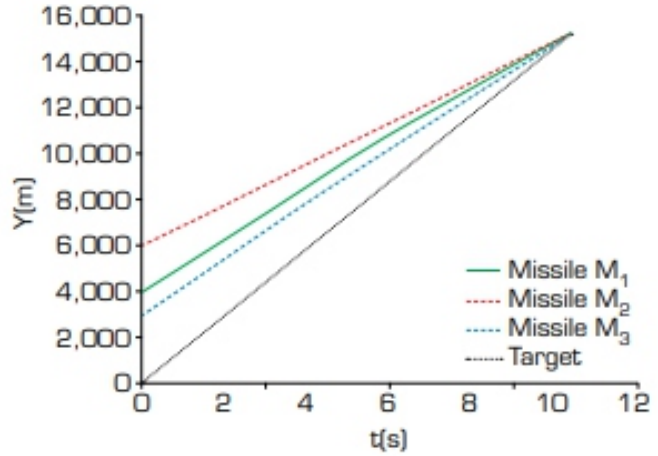


Source: Elaborated by the authors.

**Figure 6.** Change in the Y-coordinate.

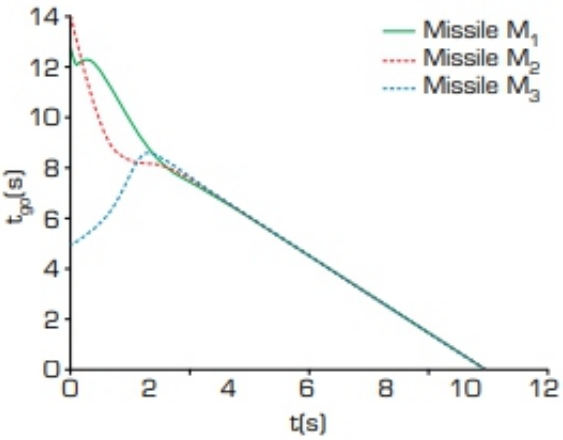


Source: Elaborated by the authors.

**Figure 7.** Time-to-go.

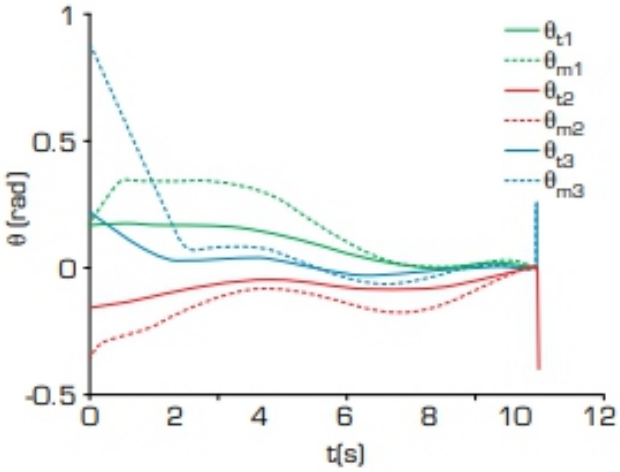


Source: Elaborated by the authors.

**Figure 8.** Lead angle $\theta$.

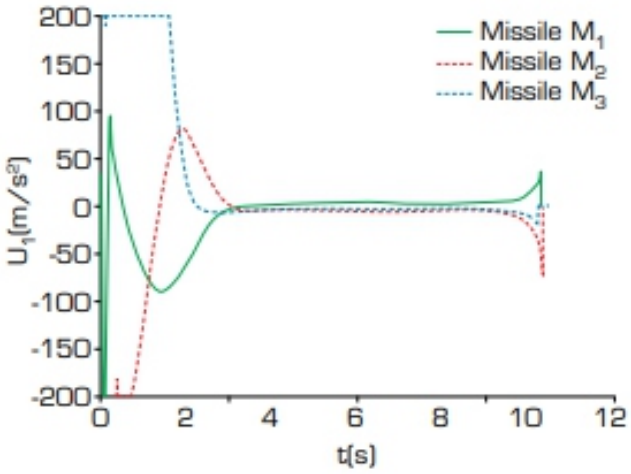


Source: Elaborated by the authors.

**Figure 9.** Acceleration command $u_1$.

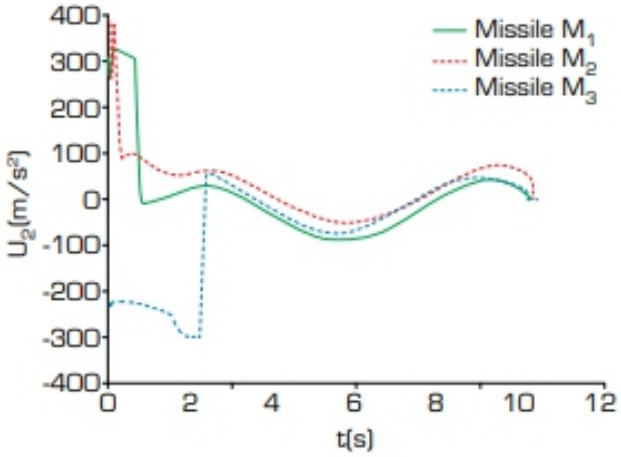


Source: Elaborated by the authors.

**Figure 10.** Acceleration command $u_2$.

Figure 3 shows the distances between the three missiles and the target, from which although the initial ranges of three missiles are different from each other greatly, they can all decrease gradually and converge to 0 at the same time. Figure 4 shows the relative motion orbit of the three missiles and the target, it can be seen that the three missiles colliding with the target at the same time. Figures 5 and 6 show the changes of missiles and target in X-coordinate and Y-coordinate. Although it can be seen from Fig. 4 that the missiles and target pass through the same coordinate position before the collision, they will not collide with each other in advance, which can be seen from Figs. 5 and 6. Because they pass through the same location at different times, the missiles do not collide with each other or with the target until the final point of encounter. Figure 7 shows the time-to-go of the three missiles, from which it can be seen that even though the time-to-go have a maximum gap of nearly 9 s at the initial moment, they reach a cooperative state after about 3 s.Figure 8 shows the lead angles of missiles and target. It can be seen from this figure that when the missile lead angle is similar to the target, it will increase to twice the target firstly, and then converge to zero in line with the target, such as missile 1. When the missile lead angle is equal to twice the target basically, it will reach twice the target lead angle quickly, and converge to zero consistent with the target, such as missile 2. When the initial missile lead angle is very different from the target, it will need to be adjusted for a long time by the guidance law to reach twice the target lead angle, and then it will converge to zero with a similar trend to the target, such as missile 3. Figure 9 shows the acceleration command along LOS. As can be seen from the figure, in the initial period of terminal guidance, the acceleration command of each missile varies greatly due to the difference of time-to-go at the initial time, but it will not change dramatically after about 3 s. That is because the time-to-go of each missile basically tends to be the same after 3 s, which can also be confirmed by Fig. 7. Figure 10 shows the acceleration command perpendicular to LOS, which indicates that each missile basically keeps the same trend after the initial adjustment, and there is no obvious chattering. At the same time, it also can be seen that the adjustment time of missile 2 is the shortest, and missile 3 is the longest, that is because the difference of initial lead angle, which also corresponds to Fig. 8. In addition, it can be seen from Figs. 9 and 10 that there is discontinuity in the commands u1 andu2, which is not acceptable in the real guidance and control system. However, the guidance law studied in this paper is based on the ideal hypothesis and is used to lay the groundwork for subsequent research, so it is acceptable here. Besides, the author will explore the problem of head-pursuit cooperative guidance law with dynamic characteristics in the further study.In addition, the guidance law proposed in this paper is represented by G1, and the head-pursuit guidance law of single missile system for comparison is represented by G2, which has the form as Eq. 42.

$$G_2 = V_m\left[-k_1 s - k_2 sig^{\lambda}(s) - (\kappa - 1)\dot{q}_i\right] \tag{42}$$

where Vm = 1200 m/s , k1 = 10, k = 0.4, λ1 = 0.9.

The statistical results of miss distance under different times of Monte Carlo simulation are shown in Table 1.

**Table 1.** Results of Monte Carlo simulation.

| Times of Monte Carlo simulation | 30 | 50 | 100 |
|---|---|---|---|
| Miss distance_$G_1$ (m) | 0.051 | 0.058 | 0.061 |
| Miss distance_$G_2$ (m) | 0.147 | 0.158 | 0.164 |

Source: Elaborated by the authors.

It can be seen from the data in the table that the miss distance of the guidance law proposed in this paper is superior to that of the comparative guidance law under different times of Monte Carlo simulation.In conclusion, the simulation results show that the guidance law proposed in this paper can make multiple missiles that have lower speed than the target carry out the head-pursuit cooperative interception against hypersonic vehicle in near space, which can provide effective theoretical guidance for the research on cooperative guidance law for near space interceptor.

## CONCLUSION

For the purpose of intercepting hypersonic vehicle in near-space, a head-pursuit cooperative guidance law based on multiagent consistency theory and sliding mode control theory is proposed in this paper, which not only intercepts the hypersonic vehicle, but also implements the coordination between missiles, thus improving the interception rate. At the same time, the selection of the reaching law and the introduction of the extended state observer not only ensure the convergence speed, but also weaken the chattering. The correctness of the guidance law is verified by Lyapunov stability theory and numerical simulations. Compared with the traditional cooperative guidance law, the head-pursuit cooperative guidance law proposed in this paper can reduce the requirement on the interceptor velocity when intercepting hypersonic targets, avoid the influence of aerodynamic thermal corrosion on the guidance accuracy, and thus achieve effective interception of hypersonic vehicle in near-space.

However, the head-pursuit cooperative guidance law is only studied in the two-dimensional plane, and its applicability in the three-dimensional case has not been verified yet. Meanwhile, the research in this paper is still at the theoretical level. Therefore, the focus of the next research will be the research on the applicability in three-dimensional environment, and the validity of the guidance law will be further verified through the hardware-in-loop simulation.

## CONFLIT OF INTEREST

Nothing to declare.

## AUTHORS' CONTRIBUTION

**Conceptualization:** Chenqi Zhu; **Methodology:** Chenqi Zhu; **Validation:** Xiang Liu; **Writing - Original Draft:** Chenqi Zhu; **Writing - Review & Editing:** Chenqi Zhu and Xiang Liu.

## DATA AVAILABILITY STATEMENT

All data sets were generated or analyzed in the current study.


## FUNDING

Not applicable.

ACKNOWLEDGEMENTS

Not applicable.


## REFERENCES


*1.Cho D, Jin KH, Tahk MJ (2015) Impact angle constrained sliding mode guidance against maneuvering target with unknown acceleration. IEEE Trans Aerosp Electron Syst 51(2):1310-1323. https://doi.org/10.1109/TAES.2015.140358*

*2.Feng LP, Fan ZE, Zhang YG (2014) Design of guidance law with impact angle and impact time constraints. C Adv Mater Res 945-949:1493-1499. https://doi.org/10.4028/www.scientific.net/AMR.945-949.1493*

*3.Feng X, Long W (2007) Reaching agreement in finite time via continuous local state feedback. Paper presented 2007 Chinese Control Conference. IEEE; Zhangjiajie, China. https://doi.org/10.1109/CHICC.2006.4347337*

*4.Golan OM, Shima T (2004) Head pursuit guidance for hypervelocity interception. AIAA 2004-4885. AIAA Guidance, Navigation, and Control Conference and Exhibit. https://doi.org/10.2514/6.2004-4885*

*5.Lee JI, Jeon IS, Tahk MJ (2007) Guidance law to control impact time and angle. IEEE Trans Aerosp Electron Syst 43(1):301-310. https://doi.org/10.1109/TAES.2007.357135*

*6.Liu KP, Cao YM, Wang SQ (2015) Terminal sliding mode control for landing on asteroids based on double power reaching law. Paper presented 2015 IEEE International Conference on Information and Automation. IEEE; 7.Lijiang, China. https://doi.org/10.1109/ICInfA.2015.7279696*

*8.Liu X, Liang XG (2019) Integrated guidance and control of multiple interceptor missiles based on improved distributed cooperative control strategy. J Aerosp Technol Manag 11(1):2119-2134. https://doi.org/10.5028/jatm.v11.1003*

*9.Shi Z, He CD, Wang SS (2018) Cooperative guidance law based on second-order sliding mode*

*control. Paper published 2018 Chinese Control And Decision Conference (CCDC). IEEE; Shenyang, China. https://doi.org/10.1109/CCDC.2018.8407333*

*10.Si YJ, Song SM (2017) Adaptive reaching law based three-dimensional finite-time guidance law against maneuvering targets with input saturation. J Aerosp Sci Technol 70(2017):198-210. https://doi.org/10.1016/j.ast.2017.08.006*

*11.Sun X, Xia YQ (2012) Optimal guidance law for cooperative attack of multiple missiles based on optimal control theory. Int J Control 85(8):1063-1070. https://doi.org/10.1080/00207179.2012.675519*

*12.Yu SH, Yu XH, Shirinzadeh BJ, Man ZH (2005) Continuous finite-time control for robotic manipulators with terminal sliding mode. J Automatica 41(11):1957-1964. https://doi.org/10.1016/j.automatica.2005.07.001*

*13.Zhang YA, Wu HL, Liu JM, Sun YM (2018) A blended control strategy for intercepting high-speed target in high altitude. JProc Inst Mech Eng G J Aerosp Eng 323(12):2263-2285. https://doi.org/10.1177/0954410017718569*

*14.Zhao EJ, Chao T, Wang SY, Yang MZ (2016) Guidance law based on finite time consensus theory for simultaneous arrival. Paper presented 2016 35th Chinese Control Conference (CCC). IEEE. Chengdu, China. https://doi.org/10.1109/ChiCC.2016.7554215*

*15.Zhu CQ (2021a) Design of head pursuit guidance law based on fractional-order sliding mode theory. J Aerosp Technol Manag 13:e0721. https://doi.org/10.1590/jatm.v13.1201*

*15.Zhu CQ (2021b) Design of finite-time guidance law based on observer and head-pursuit theory. J Proc Inst Mech Eng G J Aerosp Eng 235(13):1791-1802. https://doi.org/10.1177/0954410020984562*

*16.Zhu CQ, Guo ZY (2019) Design of head-pursuit guidance law based on backstepping sliding mode control. IOP Conf Ser: Mater Sci Eng 563:042076. https://doi.org/10.1088/1757-899x/563/4/042076*

*17.Zhu Z, Xu D, Liu JM, Xia YQ (2013) Missile guidance law based on extended state observer. IEEE Trans Ind Electron 60(12):5882-5891. https://doi.org/10.1109/TIE.2012.223225*

# Recent Advances in Solar Cells for Aerospace Applications: Materials and Technologies

**Rodrigo Savio Pessoa1 , Mariana Amorim Fraga2**

1. Departamento de Ciência e Tecnologia Aeroespacial , Instituto Tecnológico de Aeronáutica, epartamento de Física, São José dos Campos, SP, Brazil. 2. Universidade Presbiteriana Mackenzie , Escola de Engenharia, São Paulo, SP, Brazil.

This editorial provides a comprehensive overview of the latest advances in solar cell material research and the potential applications of these materials in space. The overview highlights the need for a multidisciplinary approach that considers materials, manufacturing and integration to further promote the use of solar energy in space and support the growth of programs like megaconstellations of satellites.

Solar cells play a critical role in the shift towards a future with cleaner and more sustainable energy. As the demand for renewable energy sources grows, solar cells are being increasingly utilized in various industries, including aerospace and terrestrial solar power plants, as well as in portable electronic devices (Safyanu et al. 2019). However, operating solar cells in space poses significant challenges, particularly for aerospace applications. These challenges include exposure to intense radiation, which can reduce solar cell performance and its lifespan, as well as sudden and extreme temperature changes in space, which can cause damage to the cells or malfunctions. Furthermore, space debris, such as micrometeoroids, can cause physical damage to the cells and affect their ability to produce energy. To ensure the reliability and longevity of solar cells in space, it is essential to overcome these challenges via the continued advancement of their technology.

Solar cells are widely used to supply electrical power to space missions that can last for several years. Some examples of applications are illustrated in Fig. 1. As the space exploration industry grows and more satellites are deployed for various purposes, including telecommunications and earth observation, the need for high-performance and more durable solar cells has become increasingly urgent. To meet this demand, the field of solar cell technology has invested in continuous research and development (R&D), focusing on improving photovoltaic materials and the processes used to synthesize them.

Nowadays, the most widely used photovoltaic materials in solar cells include silicon-based materials, such as monocrystalline and polycrystalline silicon, and thin-film materials, such as copper indium gallium selenide (CIGS) and gallium arsenide (GaAs) (Safyanu et al. 2019; Verduci et al. 2022). Despite their widespread use, these traditional photovoltaic materials have limitations, such as high production costs, low light-to-electricity conversion efficiency, and low durability. To overcome these challenges, researchers are exploring using new materials with the potential to revolutionize the solar cell industry through their low cost and high efficiency (Fig. 2).

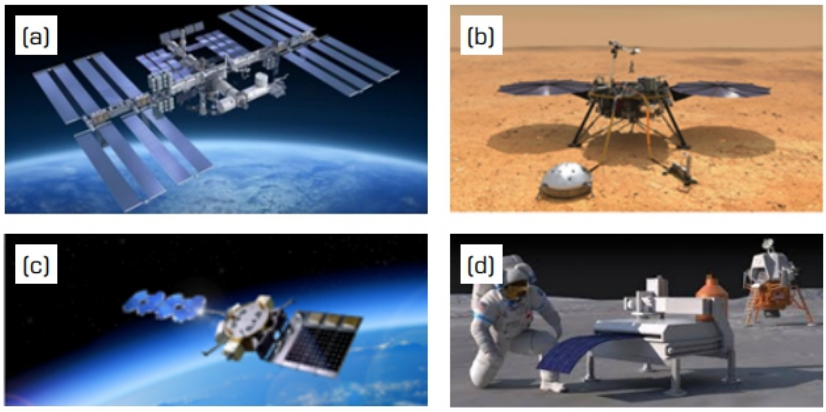


**Figure 1**. Illustrations of potential solar cell applications: (a) International Space Station powered by solar panels (Solar Cell, 2022), (b)NASA's InSight Lander robot, powered by solar energy, and holder of the off-world record of power generation (Bernardes et al. 2021) , (c) Air Force Research Laboratory's Arachne flight experiment in orbit (Space News, 2022) and (d) a lunar lander vehicle with sequential in-space printing of a perovskite solar module (McMillon-Brown et al. 2022).

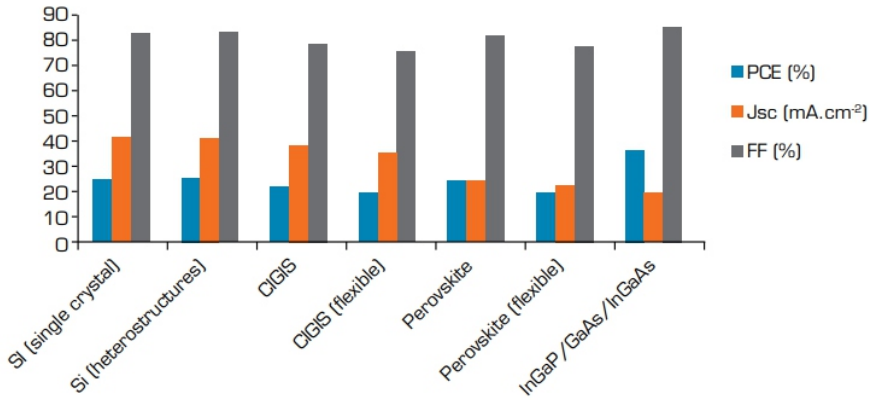


**Figure 2.** Comparison among photovoltaic material technologies. PCE = Power Conversion Efficiency, Jsc = Solar cell short-circuit density, and FF = Fill Factor.

One such material that has garnered much attention in recent years is perovskite (Verduci et al. 2022). These crystals are synthesized from low-cost and abundant elements, such as lead and tin, and have shown exceptional promise in solar cell research and development. Perovskites boast a high absorption coefficient, can absorb a wide range of light and have a high light-toelectricity conversion efficiency of around 25.5%. Additionally, perovskite-based solar cells have emerged as promising candidates for aerospace power systems due to their appealing properties, such as flexibility, cost-effective manufacturing, lightweight and exceptional radiation resistance (McMillon-Brown et al. 2022).

In recent years, using 2D materials, such as graphene and MXenes (e.g., Ti3C2Tx), in solar cell electrodes has garnered significant attention. They have been tested under space-relevant conditions as components of electronic devices such as transistors and sensors. Despite their thin structure, they have

shown remarkable resistance to high-energy particles, including electrons, protons, and gamma rays. This resistance, combined with their potential for high-efficiency photovoltaic conversion, makes 2D material-based solar cells a promising technology for future space applications (Solar Cell, 2022).

The technology used in solar cell fabrication is of paramount importance in producing solar cells for the aerospace industry. Two of the most widely used techniques are screen printing for silicon-based cells and deposition for thin-film cells. Screen printing involves the transfer of a layer of conductive material onto a substrate using a stencil or mesh screen. This method is particularly suitable for creating large, intricate designs with consistent accuracy and precision. On the other hand, deposition utilizes physical or chemical processes to deposit thin layers of materials, such as silicon, oxides and metals, onto a substrate, which are essential components of solar cell fabrication. Recently, new and innovative fabrication techniques, such as roll-to-roll processing and solution processing, have emerged through advances in technology. These state-of-the-art methods offer improved efficiency, cost-effectiveness, and the ability to produce large-area solar cells, thus making them ideal for aerospace applications where weight and cost are critical factors. Incorporating advanced fabrication techniques has opened new avenues for integrating solar cells into aerospace systems, a crucial step towards the growth of market segments such as mega-constellation programs and telecommunications satellites.

The design and integration of solar cells are critical factors in maximizing their efficiency in aerospace applications.State-of-the-art III-V multijunction solar cells are widely considered the most advanced photovoltaic technology for space use due to their high power conversion efficiency (PCE) and radiation resistance (Verduci et al. 2022). Integrating these solar cells with other essential components, such as energy storage systems, can enhance the reliability and autonomy of satellite and propulsion systems, thus leading to seamless and efficient performance. The combination of materials, fabrication techniques, and integrated design is crucial in ensuring the optimal performance of solar cells in the demanding environment of aerospace applications.In conclusion, the role of solar cells in the shift towards a greener future for energy production cannot be overstated. These cells are vital in various industries, especially aerospace, where they power satellites and other space missions. The unique conditions in space, such as intense radiation, extreme temperature changes, and space debris, pose significant challenges to solar cell performance and durability. To tackle these challenges, the field of solar cell technology is constantly evolving, with researchers exploring new materials like perovskites and 2D materials that offer improved efficiency and cost-effectiveness. The development of advanced fabrication techniques, such as roll-to-roll processing and solution processing, has paved the way for integrating solar cells into aerospace systems, making them a critical component of the space industry. The interplay of materials, fabrication techniques and integrated design is crucial for ensuring the optimal performance of solar cells in the harsh environment of aerospace applications. As we continue to move towards a more sustainable energy future, solar cells will play a vital role in powering our world

and beyond.

## REFERENCES

*1.Bernardes S, Lameirinhas RAM, Torres JPN, Fernandes CAF (2021) Characterization and Design of Photovoltaic Solar Cells That Absorb Ultraviolet, Visible and Infrared Light. Nanomaterials. Vol 11, n1, p 78. https://doi.org/10.3390/nano11010078*

*2.McMillon-Brown L, Luther JM, Peshek TJ (2022) What Would It Take to Manufacture Perovskite Solar Cells in Space? ACS Energy Letters vol. 7, no. 3 pp 1040–1042. https://doi.org/10.1021/acsenergylett.2c00276*

*3.Safyanu BD, Mohd NA, Zamri O (2019) Review of Power Device for Solar-Powered Aircraft Applications. Journal of Aerospace Technology and Management, vol.11, https://doi.org/10.5028/jatm.v11.1077*

*4.Solar Cell, 2022. EMWorks.https://www.emworks.com/application/solar-cell. Acessed on 2oth Feb 2023.*

*5.Space News, 2022. Space news. https://spacenews.com/northrop-grumman-tests-space-solar-power/. Acessed on 20th Feb 2023.*

*6.Verduci R, Romano V, Brunetti G, Nia NY, Di Carlo A, D'Angelo G, Ciminelli C (2022). Solar Energy in Space Applications: Review and Technology Perspectives. Advanced Energy Materials vol. 12, no. 29. https://doi.org/10.1002/aenm.20220012*

# Instructions for Authors

**Essentials for Publishing in this Journal**

1 Submitted articles should not have been previously published or be currently under consideration for publication elsewhere.

2 Conference papers may only be submitted if the paper has been completely re-written (taken to mean more than 50%) and the author has cleared any necessary permission with the copyright owner if it has been previously copyrighted.

3 All our articles are refereed through a double-blind process.

4 All authors must declare they have read and agreed to the content of the submitted article and must sign a declaration correspond to the originality of the article.

**Submission Process**

All articles for this journal must be submitted using our online submissions system. http://enrichedpub.com/ . Please use the Submit Your Article link in the Author Service area.

**Manuscript Guidelines**

The instructions to authors about the article preparation for publication in the Manuscripts are submitted online, through the e-Ur (Electronic editing) system, developed by **Enriched Publications Pvt. Ltd**. The article should contain the abstract with keywords, introduction, body, conclusion, references and the summary in English language (without heading and subheading enumeration). The article length should not exceed 16 pages of A4 paper format.

**Title**

The title should be informative. It is in both Journal's and author's best interest to use terms suitable. For indexing and word search. If there are no such terms in the title, the author is strongly advised to add a subtitle. The title should be given in English as well. The titles precede the abstract and the summary in an appropriate language.

**Letterhead Title**

The letterhead title is given at a top of each page for easier identification of article copies in an Electronic form in particular. It contains the author's surname and first name initial .article title, journal title and collation (year, volume, and issue, first and last page). The journal and article titles can be given in a shortened form.

**Author's Name**

Full name(s) of author(s) should be used. It is advisable to give the middle initial. Names are given in their original form.

**Contact Details**

The postal address or the e-mail address of the author (usually of the first one if there are more Authors) is given in the footnote at the bottom of the first page.

**Type of Articles**

Classification of articles is a duty of the editorial staff and is of special importance. Referees and the members of the editorial staff, or section editors, can propose a category, but the editor-in-chief has the sole responsibility for their classification. Journal articles are classified as follows:

**Scientific articles:**

1. Original scientific paper (giving the previously unpublished results of the author's own research based on management methods).

2. Survey paper (giving an original, detailed and critical view of a research problem or an area to which the author has made a contribution visible through his self-citation);

3. Short or preliminary communication (original management paper of full format but of a smaller extent or of a preliminary character);

4. Scientific critique or forum (discussion on a particular scientific topic, based exclusively on management argumentation) and commentaries. Exceptionally, in particular areas, a scientific paper in the Journal can be in a form of a monograph or a critical edition of scientific data (historical, archival, lexicographic, bibliographic, data survey, etc.) which were unknown or hardly accessible for scientific research.

**Professional articles:**

1. Professional paper (contribution offering experience useful for improvement of professional practice but not necessarily based on scientific methods);
2. Informative contribution (editorial, commentary, etc.);
3. Review (of a book, software, case study, scientific event, etc.)

**Language**

The article should be in English. The grammar and style of the article should be of good quality. The systematized text should be without abbreviations (except standard ones). All measurements must be in SI units. The sequence of formulae is denoted in Arabic numerals in parentheses on the right-hand side.

**Abstract and Summary**

An abstract is a concise informative presentation of the article content for fast and accurate Evaluation of its relevance. It is both in the Editorial Office's and the author's best interest for an abstract to contain terms often used for indexing and article search. The abstract describes the purpose of the study and the methods, outlines the findings and state the conclusions. A 100- to 250-Word abstract should be placed between the title and the keywords with the body text to follow. Besides an abstract are advised to have a summary in English, at the end of the article, after the Reference list. The summary should be structured and long up to 1/10 of the article length (it is more extensive than the abstract).

**Keywords**

Keywords are terms or phrases showing adequately the article content for indexing and search purposes. They should be allocated heaving in mind widely accepted international sources (index, dictionary or thesaurus), such as the Web of Science keyword list for science in general. The higher their usage frequency is the better. Up to 10 keywords immediately follow the abstract and the summary, in respective languages.

**Acknowledgements**

The name and the number of the project or programmed within which the article was realized is given in a separate note at the bottom of the first page together with the name of the institution which financially supported the project or programmed.

**Tables and Illustrations**

All the captions should be in the original language as well as in English, together with the texts in illustrations if possible. Tables are typed in the same style as the text and are denoted by numerals at the top. Photographs and drawings, placed appropriately in the text, should be clear, precise and suitable for reproduction. Drawings should be created in Word or Corel.

**Citation in the Text**

Citation in the text must be uniform. When citing references in the text, use the reference number set in square brackets from the Reference list at the end of the article.

**Footnotes**

Footnotes are given at the bottom of the page with the text they refer to. They can contain less relevant details, additional explanations or used sources (e.g. scientific material, manuals). They cannot replace the cited literature.
The article should be accompanied with a cover letter with the information about the author(s): surname, middle initial, first name, and citizen personal number, rank, title, e-mail address, and affiliation address, home address including municipality, phone number in the office and at home (or a mobile phone number). The cover letter should state the type of the article and tell which illustrations are original and which are not.

**Address of the Editorial Office:**

**Enriched Publications Pvt. Ltd.**
**S-9,**IInd FLOOR, MLU POCKET,
MANISH ABHINAV PLAZA-II, ABOVE FEDERAL BANK,
PLOT NO-5, SECTOR -5, DWARKA, NEW DELHI, INDIA-110075,
PHONE: - + (91)-(11)-45525005